SEDIMENTOLOGY the journal of the International Association of Sedimentologists

Sedimentology (2022) **69**, 1953–1991 doi: 10.1111/sed.12978

Recognizing key sedimentary facies and their distribution in mixed turbidite–contourite depositional systems: The case of the Pacific margin of the Antarctic Peninsula

SARA RODRIGUES*, FRANCISCO JAVIER HERNÁNDEZ-MOLINA*, CLAUS-DIETER HILLENBRAND†, RENATA G. LUCCHI‡'§, FRANCISCO J. RODRÍGUEZ-TOVAR¶, MICHELE REBESCO‡ and ROBERT D. LARTER†

**Department of Earth Sciences, Royal Holloway University of London, Egham Surrey, TW20 0EX, UK (E-mail: Sara.Rodrigues.2017@live.rhul.ac.uk)*

†British Antarctic Survey, High Cross Madingley Road, Cambridge, CB3 0ET, UK

‡Istituto Nazionale di Oceanografia e di Geofisica Sperimentale, Borgo Grotta Gigante, Trieste, 42/c 34010, Italy

§Centre for Arctic Gas Hydrate, Environment and Climate, UiT, The Arctic University of Norway, Naturfagbygget Dramsveien, 201 9010 Tromsø, Norway

¶Departamento de Estratigrafía y Paleontología, Universidad de Granada, 18002 Granada, Spain

Associate Editor – Victoria Valdez

ABSTRACT

Interplay of deep-water sedimentary processes is responsible for building a myriad of features and deposits across mixed turbidite–contourite systems, from <5 cm beds to >200 km long sedimentary drifts. Investigations of the spatial and temporal variability of their sedimentary facies and facies associations is crucial to reveal the dynamics between along-slope bottom currents and down-slope turbidity currents, as well as their impact on drift construction and channel erosion. This study focuses on extensive modern mixed (turbidite–contourite) systems, developed across the continental rise of the Pacific margin of the Antarctic Peninsula. Nine sediment cores were sampled and analysed, through grain size and geochemical methods, to study the sedimentary facies at high-resolution (*ca* 1 to 20 cm). Three main facies associations have been identified across distinct morphological features (i.e. mounded drifts and trunk channels), comprising intercalations of hemipelagites, bottom current reworked sands (which include fine to coarse-grained contourites) and gravitational facies (turbidites and mass-transport deposits). These facies associations reflect fluctuations of the background sedimentation, oscillations of the bottom-current velocity and of the frequency of gravity-driven currents. The sedimentary record features cyclic alternations during the Late Quaternary (>99 kyr), suggesting that variations between along-slope bottom currents and down-slope turbidity currents are strongly linked to glacial–interglacial cycles during Marine Isotope Stages 1 to 6. Sedimentary records affected by bottom currents on polar margins, such as those of the Antarctic Peninsula, are essential to decipher the facies and facies sequences of bottom-current deposits, as the low degree of bioturbation throughout most of the sediments allows us to observe the original sedimentary structures, which are poorly preserved in similar deposits from other continental margins.

Keywords Antarctic Peninsula, contourite, Late Quaternary, mixed and hybrid systems, sediment cores, turbidite.

© 2022 The Authors. *Sedimentology* published by John Wiley & Sons Ltd on behalf of International Association of Sedimentologists

This is an open access article under the terms of the Creative Commons Attribution License, which permits use, distribution and reproduction in any medium, provided the original work is properly cited.

INTRODUCTION

A common challenge in deep-sea research is the distinction of multiple sedimentary facies within a complex depositional environment. The mixing and interplay between several deep-water sedimentary processes hinders their recognition, particularly in settings dominated by fine-grained sediments. Along-slope bottom currents and down-slope turbidity currents are considered two of the main multi-scale drivers responsible for the formation of distinct sedimentary facies and stratigraphic stacking patterns across pure (i.e. contourite or turbidite) and/or mixed turbidite–contourite systems (Faugères *et al.*, 1999; Rebesco *et al.*, 2014; Fonnesu *et al.*, 2020; Rodrigues *et al.*, 2021). Thus, deep-marine systems are characterized by numerous features and deposits built by the interplay of bottom current entrainment and winnowing, turbidity current overspill and continuous hemipelagic settling.

However, the establishment of clear, diagnostic criteria for mixed depositional systems has been the focus of a debate during the last decades (Shanmugam, 1997, 2017; Mulder *et al.*, 2008; Stow & Smillie, 2020). Several authors have identified contourite deposits based on the presence and abundance of bioturbation (Stow, 1982; Gonthier *et al.*, 1984; Stow & Faugères, 2008), whereas others have emphasized the importance of primary sedimentary structures (Shanmugam *et al.*, 1993; Stanley, 1993; Martín-Chivelet *et al.*, 2008). Furthermore, past sedimentological studies of turbidite deposits, in ancient records and in modern environments, have called into question the previously established criteria for turbidites (Shanmugam, 1997, 2016). These studies have proposed new conceptual models (Lowe, 1982; Haughton *et al.*, 2009; Stow & Smillie, 2020; Zhang *et al.*, 2020) and highlighted the significance of interaction or alternation in sedimentary processes (Mutti, 2011; de Castro *et al.*, 2020, 2021). Mulder *et al.* (2008) suggested that interactions between turbidity and bottom currents can generate three distinct types of deposits: (i) alternations of turbidites and contourites (Stow *et al.*, 1998; Michels *et al.*, 2002; Brackenridge *et al.*, 2013); (ii) redistributed or reworked gravity-driven deposits (Mutti, 1992; Stow *et al.*, 2002; Hanquiez *et al.*, 2010; Gong *et al.*, 2013); and (iii) synchronous (mixed or hybrid) deposits (Sansom, 2018; Fonnesu *et al.*, 2020; Fuhrmann *et al.*, 2020). However, the full range of their lateral and vertical associations remains unknown. In fact, several authors have identified transitional facies between the previously described examples and proposed additional modifications to the currently known models (Shanmugam, 2016, 2017; de Castro *et al.*, 2020; Stow & Smillie, 2020; de Weger *et al.*, 2021).

There is a significant interest in the recognition and distinction of deep-water facies due to their impact on the formation of hydrocarbon reservoirs (Viana, 2008; Mutti *et al.*, 2014; Sansom, 2018; Fonnesu *et al.*, 2020), as well as their usefulness as records of palaeoclimatic or palaeoceanographic changes (Rebesco *et al.*, 2014; Thiéblemont *et al.*, 2020), slope stability and geohazard studies (Laberg & Camerlenghi, 2008; Miramontes *et al.*, 2018; Teixeira *et al.*, 2019) and for the sustainability of deep-sea ecosystems (Hebbeln *et al.*, 2016; Lozano *et al.*, 2020). At present, the study of mixed systems has focused strongly on the recognition of seismic and morphological elements at a broad (>10 m) to medium (*ca* 1 m) scale (Michels *et al.*, 2002; Gong *et al.*, 2013; Mutti *et al.*, 2014; Creaser *et al.*, 2017; Cauxeiro *et al.*, 2020; Pandolpho *et al.*, 2021; Rodrigues *et al.*, 2021). However, several authors have underlined a clear dearth of studies at the sedimentary facies scale (Stanley, 1987, 1988, 1993; Shanmugam *et al.*, 1993; Viana *et al.*, 1998; Gong *et al.*, 2016). A fine-scale analysis of mixed or hybrid systems is needed to better understand the spatial and temporal variability of their deposits and to link their formation to the complex mixing of deep-water processes.

The Pacific margin of the Antarctic Peninsula (PMAP) holds extensive mixed depositional systems (Fig. 1A), characterized by complex sedimentary features and diverse sedimentary facies (Pudsey & Camerlenghi, 1998; Lucchi *et al.*, 2002; Lucchi & Rebesco, 2007; Venuti *et al.*, 2011; Hillenbrand *et al.*, 2021). The PMAP provides a first-class perspective to better understand the lateral and vertical distribution of mixed depositional systems as it contains one of the largest modern examples in existence, offering new insights into the interaction between along-slope and down-slope processes. Thus, the objectives of this work are: (i) to identify and discriminate key sedimentary facies and facies associations; (ii) characterize the spatial and temporal variability of these facies and their relation to the distinct morphological elements; and (iii) decipher the controlling factors behind their formation and their influence in the

© 2022 The Authors. *Sedimentology* published by John Wiley & Sons Ltd on behalf of International Association of Sedimentologists, *Sedimentology*, **69**, 1953–1991

development of mixed systems. The present results will not only contribute to the establishment and recognition of diagnostic criteria for sedimentary facies and facies associations developed in mixed depositional systems, but also provide a deeper understanding of the PMAP mixed systems and their development during the Late Quaternary.

GEOLOGICAL AND OCEANOGRAPHIC SETTINGS

Geological and morphological framework

The south-west part of the PMAP is a passive continental margin (Fig. 1). However, the PMAP used to be an active margin as far back as the Early Cretaceous, due to the subduction of the Phoenix Plate below the Antarctic Plate (Pankhurst, 1990; Poblete *et al.*, 2011; Nerlich *et al.*, 2013). The migration of the Antarctic–Phoenix spreading ridge towards the trench that ran along the PMAP resulted in ridge-crest trench collisions. As each ridge segment arrived at the trench, subduction ended along that section of the margin, and thus the south-west part of the PMAP became passive progressively from the middle Eocene to the Pliocene. Subsequent thermal decay, sediment deposition and compaction led to a gradual subsidence until the present day (Larter & Barker, 1989, 1991; Larter *et al.*, 1997).

At present, the PMAP is characterized by distinct physiographic domains, with different structural and morphological features (Fig. 1B). The continental shelf of the PMAP dips landward (0° to 1°) from the shelf break to the coast and has an average water depth of 500 m (Fig. 1A). The shelf is characterized by several cross-shelf bathymetric troughs separated by banks (or highs; Larter *et al.*, 1997; Livingstone *et al.*, 2012; Ó Cofaigh *et al.*, 2014; Lavoie *et al.*, 2015). The banks are generally associated with underlying structural or basement highs (Larter *et al.*, 1997; Rebesco *et al.*, 1998; Hernández-Molina *et al.*, 2017), whereas the troughs usually form broad U-shaped, WNW–ESE to north–south elongated depressions (Fig. 1A). These features terminate at a steep continental slope (10° to 13°), which extends between 500 m and 3000 m water depth (Fig. 1A) and is incised by numerous north-west/south-east oriented gullies between 550 m and 1600 m water depth (Vanneste & Larter, 1995; Dowdeswell *et al.*, 2004; Heroy & Anderson, 2005; Gales *et al.*, 2013). Below the steep slope, the continental rise forms an extensive domain between 3000 m and 4500 m water depth (Tucholke & Houtz, 1976; Tucholke, 1977). The continental rise hosts the mixed turbidite–contourite systems (Fig. 1A), characterized by distinct depositional and erosional features (Rebesco *et al.*, 1996, 1998, 2002; Hernández-Molina *et al.*, 2017). The mixed systems comprise 13 large, mounded drifts between 2300 m and 3900 m water depth (Fig. 1A), which are separated by 12 north-west/south-east oriented trunk channels (Fig. 1A; Tomlinson *et al.*, 1992; Rebesco *et al.*, 1996, 1998, 2002; Dowdeswell *et al.*, 2004; Amblas *et al.*, 2006; Hernández-Molina *et al.*, 2017). The mounded drifts exhibit variable morphology due to the presence of channels and gullies across their proximal flanks (Fig. 1B) and also of gravitational scars across the steep south-west flanks, and more rarely on the gently dipping north-east flanks (Rebesco *et al.*, 1998, 2002; Volpi *et al.*, 2011; Larter *et al.*, 2019). A dendritic channel network at *ca* 2500 m water depth feeds into the large trunk channels (Tomlinson *et al.*, 1992; Rebesco *et al.*, 2002; Amblas *et al.*, 2006), forming north-east/south-west to north-west/south-east erosional features across the lower slope and upper continental rise (Fig. 1B). These features are often associated with channel overbank deposits across intra-channel areas (Fig. 1B), which appear as symmetrical to asymmetrical 'bar' shapes, usually parallel to the channel system trend (Fig. 1B). Gravitational deposits, such as mass-transport deposits (MTDs), debrites and turbidites have also been identified within the complex channel systems and across the mounded drifts (Amblas *et al.*, 2006; Diviacco *et al.*, 2006; Lucchi & Rebesco, 2007; Rebesco & Camerlenghi, 2008; Volpi *et al.*, 2011).

Modern circulation

The Southern Ocean is characterized by one of the largest ocean currents, the Antarctic Circumpolar Current (ACC), which is driven eastward by strong wind stresses (Fig. 1A). The ACC reaches an average net baroclinic transport of 173 Sv (1 Sv equals 10^6 m^3 s^{-1}) as it flows through the Drake Passage (Donohue *et al.*, 2016). The ACC also has several bottom-reaching fronts, which dip preferentially towards the north (Naveira Garabato *et al.*, 2002, 2003). However, the oceanic circulation of deep and bottom waters along the PMAP comprises mainly Circumpolar Deep Water (CDW) and its

© 2022 The Authors. *Sedimentology* published by John Wiley & Sons Ltd on behalf of International Association of Sedimentologists, *Sedimentology*, **69**, 1953–1991

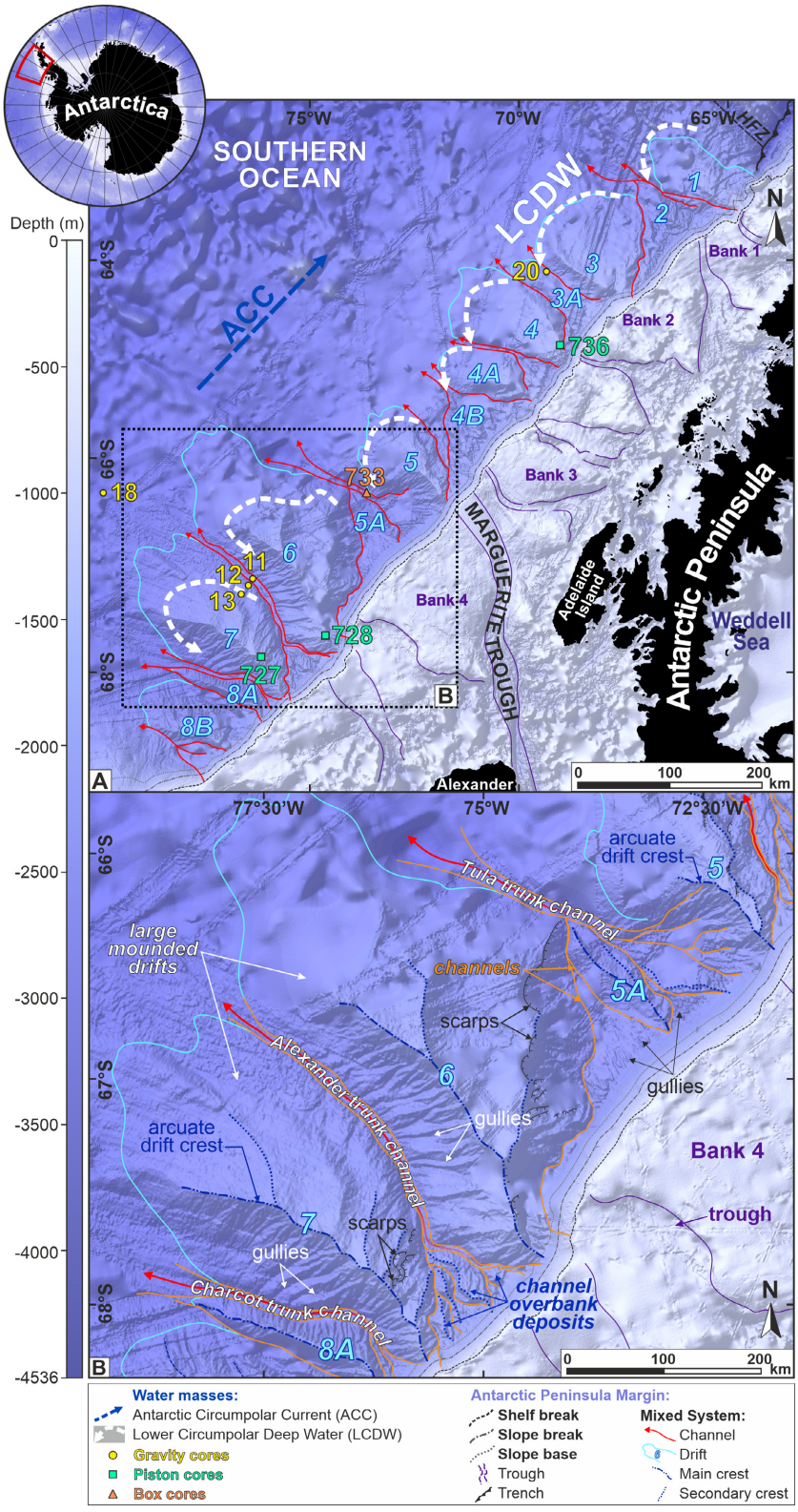

Fig. 1. Location of the modern mixed depositional systems and schematic deep ocean circulation on the Pacific margin of the Antarctic Peninsula (PMAP). Oceanographic circulation after Orsi *et al.* (1995, 1999), Giorgetti *et al.* (2003), Hillenbrand *et al.* (2008a), Palmer *et al.* (2012) and Hernández-Molina *et al.* (2017). This map is based on the GEBCO gridded bathymetry (GEBCO, 2019).

© 2022 The Authors. *Sedimentology* published by John Wiley & Sons Ltd on behalf of International Association of Sedimentologists, *Sedimentology*, **69**, 1953–1991

westward directed contour currents (Fig. 1A; Camerlenghi *et al.*, 1997; Giorgetti *et al.*, 2003; Hillenbrand *et al.*, 2008a; Holland *et al.*, 2010; Palmer *et al.*, 2012).

The CDW comprises relatively warm and saline water flowing towards north-east between 200 m and 3000 m water depth (Fig. 1A). The CDW is characterized by complex and dynamic mixing during its pathway around the Antarctic continent and within the ACC (Sievers & Nowlin, 1984; Whitworth & Nowlin, 1987; Whitworth *et al.*, 1998). The CDW comprises Upper Circumpolar Deep Water (UCDW), formed mainly in the east South Pacific Ocean and the West Indian Ocean, and Lower Circumpolar Deep Water (LCDW), which derives from saline North Atlantic Deep Water (NADW) injected into the ACC in the Atlantic sector of the Southern Ocean (Fig. 1A; Patterson & Whitworth, 1990; Stramma & England, 1999; Hillenbrand *et al.*, 2008a). The CDW upwells along the PMAP, with the UCDW occupying the water column between *ca* 200 m and 1000 m water depth, and being characterized by an oxygen minimum and a temperature and nutrient maximum (see Fig. S1 for details; Ito *et al.*, 2010). Further away from the PMAP, both the UCDW and the LCDW flow towards the north-east within the ACC. At the PMAP, a branch of the LCDW originating from the Weddell Sea flows south-westward along the continental slope and upper continental rise centred at *ca* 3500 m water depth (Fig. 1A), with an average current speed of *ca* 6 cm s^{-1}, maximum speed of 20 cm s^{-1}, potential temperature of 0.11 to 0.13°C and salinity up to 34.70 psu (Camerlenghi *et al.*, 1997; Giorgetti *et al.*, 2003; Hillenbrand *et al.*, 2008a).

DATA AND METHODS

A variety of geochemical and sedimentological analyses were conducted on several sediment cores to study the sedimentary facies of the PMAP mixed systems in detail.

Sediment cores

The sediment cores were examined in collaboration with the British Antarctic Survey (BAS) and the Italian National Institute of Oceanography and Applied Geophysics (OGS). The BAS provided three piston cores and one box core (Table 1), collected during cruise JR298 in 2015 (Fig. 1A). The OGS provided five gravity cores

Table 1. Metadata and summary of analyses carried out on the sediment cores. PC: piston core; GBC: giant box core; SED: gravity core collected on behalf of the SEDANO-II Project.

Core	Length (m)	Water depth (m)	Location	Latitude	Longitude	High-resolution photographs	X-radiographs	Thin sections	Grain size	XRF scanning
SED-11	5	3725	Alexander channel	67°08.61′S	76°22.09′W	●		●	●	●
SED-12	6.97	3620	Base of north-east flank drift 7	67°12.48′S	76°29.45′W	●	●	●	●	●
SED-13	6.67	3559	North-east flank drift 7	67°17.16′S	76°38.80′W			●	●	
SED-18	4	4215	Alexander channel mouth	66°19.94′S	79°57.75′W	●		●	●	●
SED-20	5.09	3425	Palmer channel	64°06.41′S	69°20.11′W	●	●	●	●	●
PC727	7.57 (9.90*)	2681	Crest drift 7	67°51.86′S	76°10.76′W		●		●	●
PC728	12.17	2454	Proximal crest drift 6	67°40.10′S	74°38.54′W		●			●
GBC733	0.28	3857	Tula channel	66°22.33′S	73°42.27′W		●		●	●
PC736	9.91 (10.25*)	2325	Proximal crest drift 4	64°53.72′S	69°02.13′W		●		●	●

* Total core recovery (including flow-in in the lower parts of PCs).

© 2022 The Authors. *Sedimentology* published by John Wiley & Sons Ltd on behalf of International Association of Sedimentologists, *Sedimentology*, **69**, 1953–1991

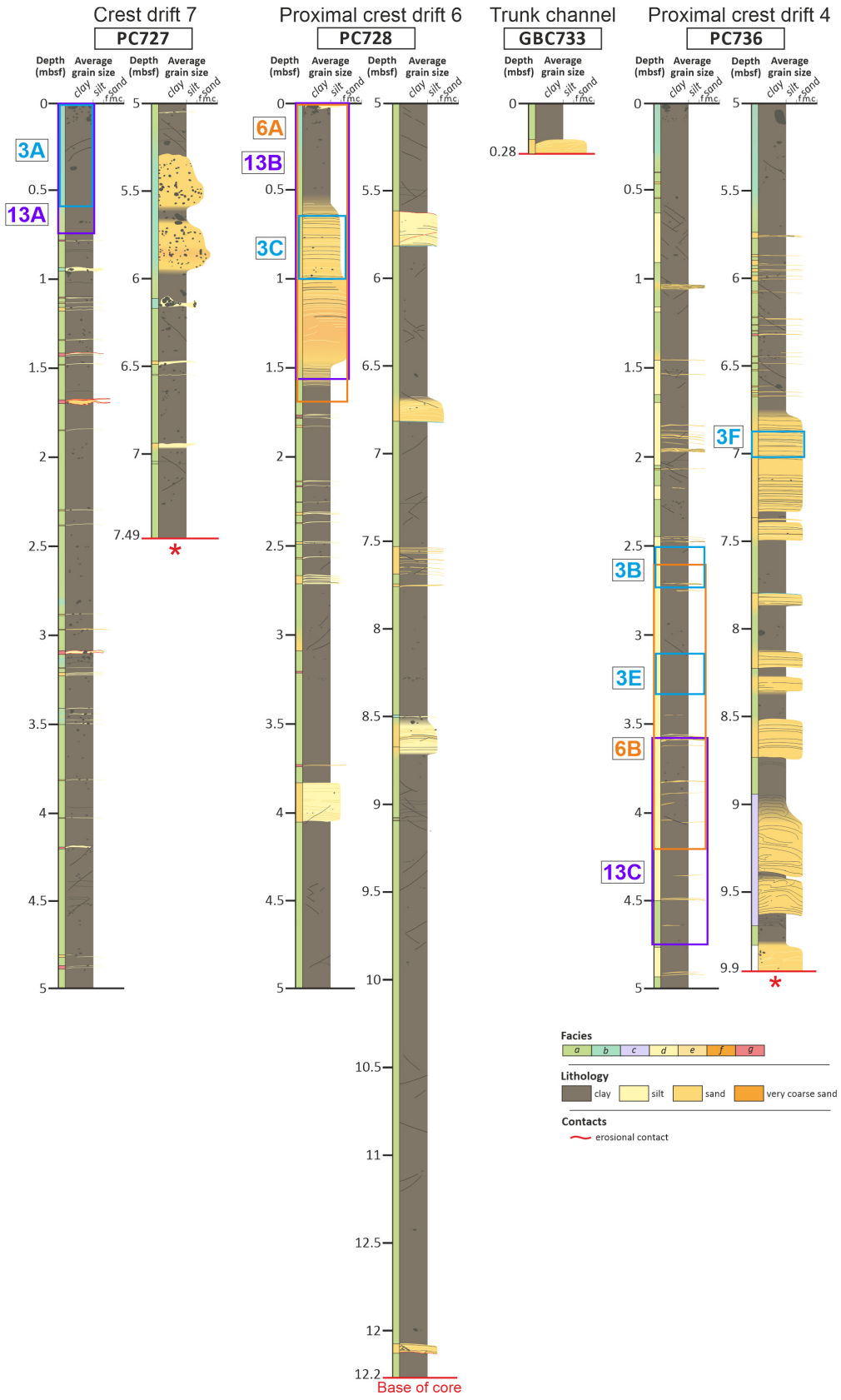

Fig. 2. (For caption see next page).

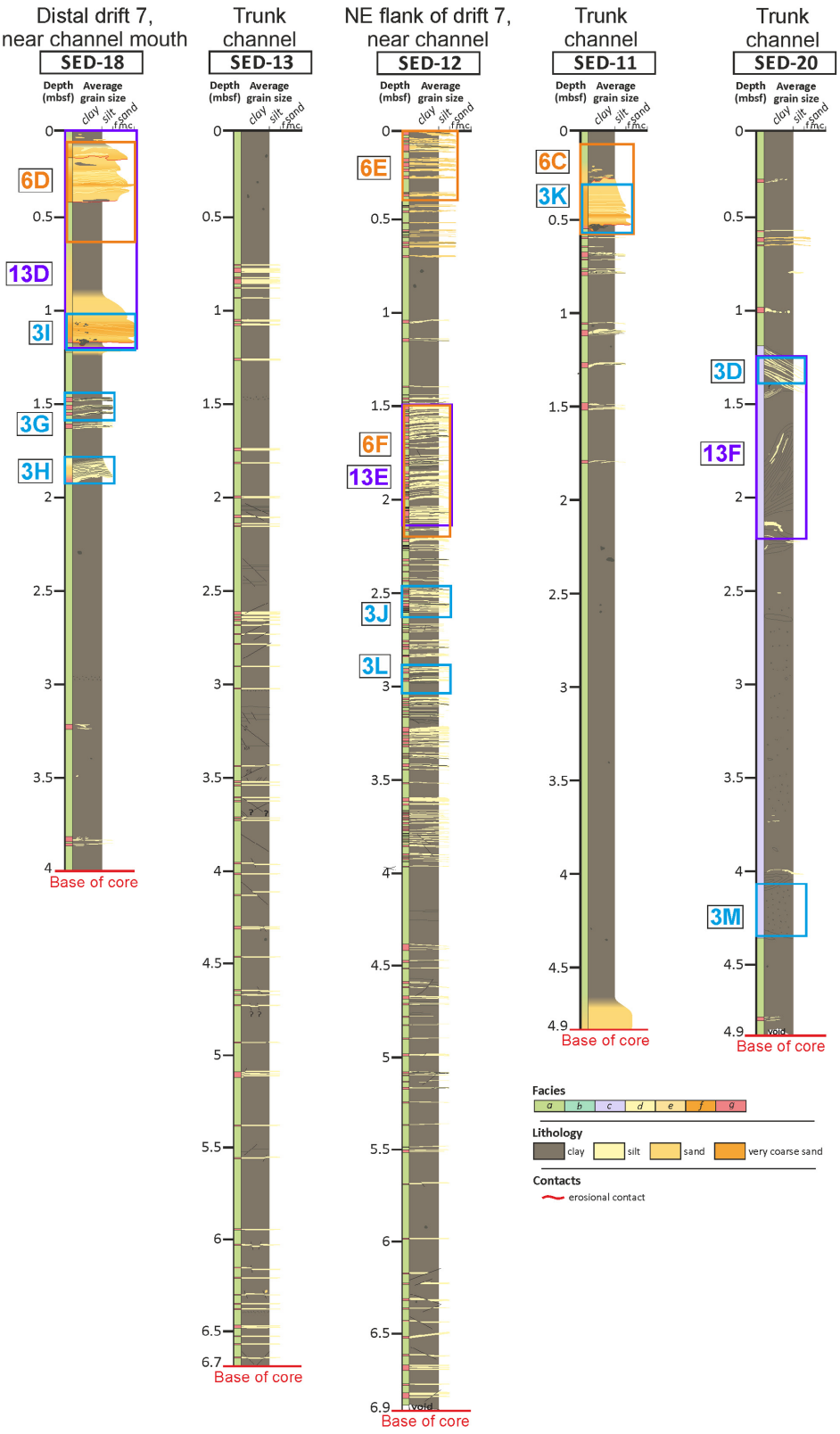

Fig. 2. Lithological and facies logs of the sediment cores examined in this study. Sparse ice-rafted debris (IRD) was not taken into consideration for the average grain size. *: core interval disturbed by flow-in at the base (not shown). Location of the cores in Fig. 1. Detailed core descriptions and interpretations in Fig. S2. Boxes 3A to 13F mark the depth ranges of high-resolution core photographs and X-radiographs shown in Figs 3, 6 and 13.

© 2022 The Authors. *Sedimentology* published by John Wiley & Sons Ltd on behalf of International Association of Sedimentologists, *Sedimentology*, **69**, 1953–1991

(Fig. 2), collected during the PNRA (Italian national program of research in Antarctica) SEDANO-II Project in 1998 (Fig. 1A). Cores SED-12 and SED-13 were taken from the north-east flank of Drift 7, while PC727 was recovered from its crest (Fig. 1A). SED-11 was collected on the Alexander Channel, between Drifts 6 and 7, whereas SED-18 was taken near the channel mouth (Fig. 1A). Furthermore, core PC728 was collected from the proximal crest of Drift 6 and PC736 was retrieved from the proximal crest of Drift 4 (Fig. 1A). Box core GBC733 was recovered from the Tula Channel between Drifts 5 and 5A (Fig. 1A), and SED-20 was taken from the Palmer Channel between Drifts 3A and 3 (Fig. 1A). The parameters analysed on each sediment core are listed in Table 1.

The sediment cores were visually described, logged and sampled for different analyses (Table 1) to study the sediment composition, lithological contacts, sedimentary structures, ichnological features, geochemical properties, and the spatial and temporal variability of each sedimentary facies.

Methodology

High-resolution core photographs and X-radiographs

High-resolution photographs and X-radiographs of the archive halves of the sediment cores were obtained during and after cruises JR298 and SEDANO-II (Fig. 3). The high-resolution photographs were taken at the Istituto di Scienze Marine of the Consiglio Nazionale delle Ricerche (ISMAR-CNR, Bologna) using a Colour Line Scan Camera (equipped with a third generation Avaatech XRF core scanner; Avaatech, Dodewaard, The Netherlands), which has a cross coverage up to 150 mm and a resolution of 70 μm. Two-dimensional X-radiographs from the archive halves of the JR298 cores were prepared at The Queen's Veterinary School Hospital, University of Cambridge (UK), whereas the X-radiographs of the SEDANO-II cores were acquired by SGP TESTING S.r.l. in Trieste (Italy). X-ray settings (energy, exposure time, etc.) were selected to obtain optimum image quality and adjusted to compensate for variations in half-core section thickness and lithology. For most core sections, three to four overlapping images were acquired and subsequently cropped and sliced. These methods aid visual core description with the identification of lithological variations and sedimentary structures.

X-ray fluorescence scanning

X-ray fluorescence (XRF) scanning was conducted on both the SEDANO-II and the JR298 cores. The JR298 cores were scanned with a third generation Avaatech XRF core scanner with a Rhodium-anode at the Department of Earth Sciences, University of Cambridge. Each section was measured at three different voltages and currents: 10 kV and 750 mA, 30 kV and 500 mA, and at 50 kV and 1000 mA. Results were previously presented in Channell *et al.* (2019) and Hillenbrand *et al.* (2021). The XRF scans on the SEDANO-II cores were carried out at ISMAR-CNR, also using an Avaatech XRF core scanner with a Rhodium-anode. This non-destructive method yields semi-quantitative elemental data for major and minor elements in total counts. The XRF scans were performed at 1 cm resolution, using voltages of 10 kV, 30 kV and 50 kV and a current of 0.4 mA. The XRF scanning results were used to study the geochemical composition of the sediments. Central log ratios (*clr*) were calculated after Aitchison (1986) and Martin-Puertas *et al.*

Fig. 3. Detailed core photographs (D to M), X-radiographs (A to F) and thin sections ('1' to '6') for the identified facies. (A) Facies-a and Facies-b with dominant *Zoophycos* (*Zo*), *Thalassinoides* (*Th*), *Planolites* (*Pl*) and local *Chondrites* (*Ch*) and U-shaped traces (U-sh), foraminifera (1) and IRD 'cap'; (B) parallel and cross-laminations in Facies-d with clay to silty sand lamina, and local occurrences of *Phycosiphon* (*Ph*) and vertical traces (vt); (C) Facies-e with parallel-laminations, local *Phycosiphon* (*Ph*) and increase of sand content and bed thickness towards its base; (D) Facies-c with tilted beds; (E) mud ripples characteristic of Facies-d with scarce *Planolites* (*Pl*); (F) parallel-laminations in Facies-e; (G) turbidite deposits with parallel-laminations of Facies-g alternating with Facies-a (4); (H) reworked turbidite deposit of Facies-g overlain by Facies-e, d and a; (I) reworked turbidite of Facies-f with cross-laminations; (J) thin-bedded turbidites with flame structures of Facies-g alternating with Facies-a (5); (K) coarse to fine-grained ('2' and '3') reworked turbidite with normal grading and parallel-laminations of Facies-f; (L) thin-bedded turbidites with parallel-laminations of Facies-g alternating with Facies-a ('6'); and (M) poorly sorted mixture of matrix and pebbles in Facies-c. Depth ranges of core intervals are given in Fig. 2.

© 2022 The Authors. *Sedimentology* published by John Wiley & Sons Ltd on behalf of International Association of Sedimentologists, *Sedimentology*, **69**, 1953–1991

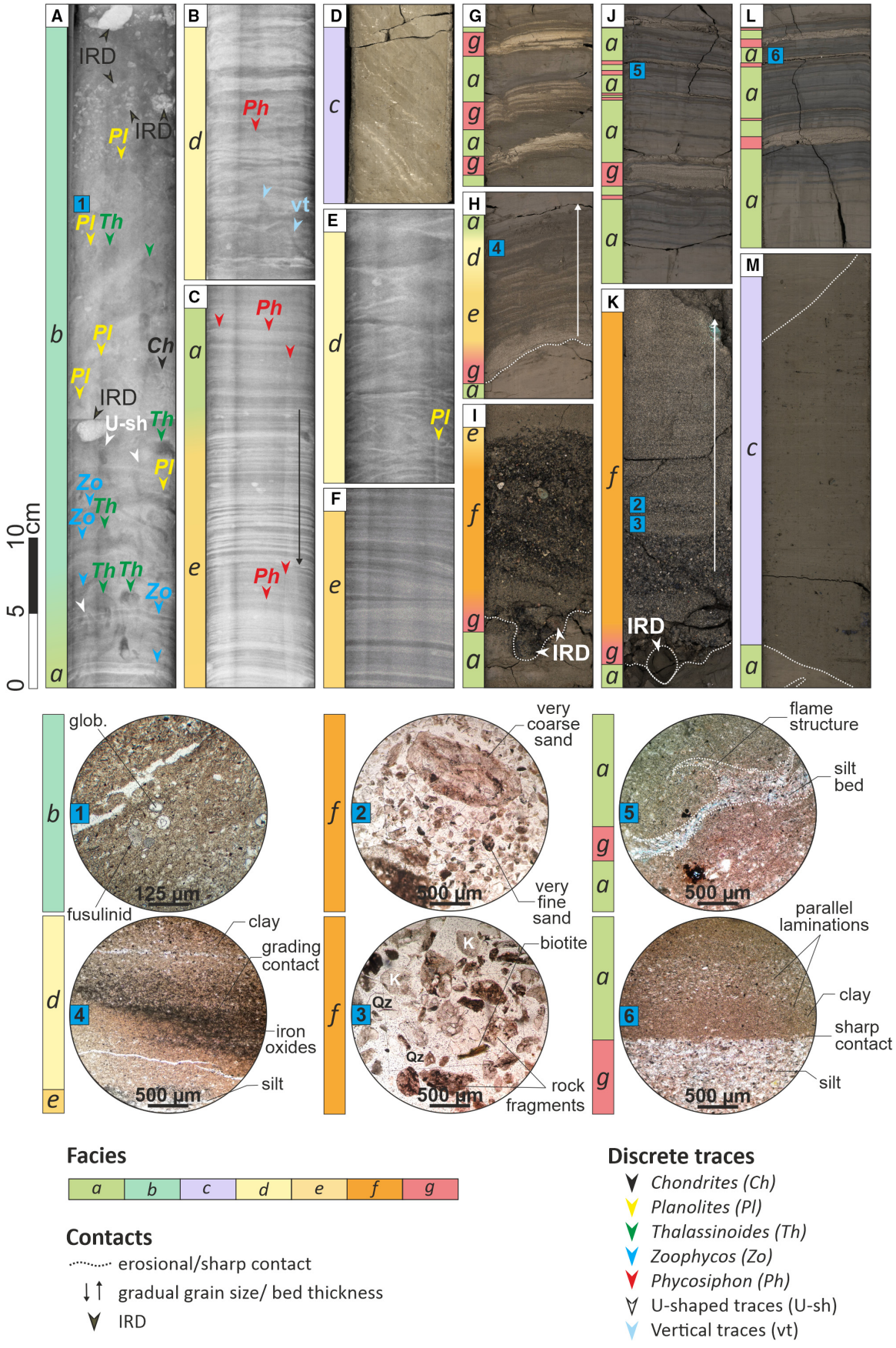

© 2022 The Authors. *Sedimentology* published by John Wiley & Sons Ltd on behalf of International Association of Sedimentologists, *Sedimentology*, **69**, 1953–1991

(2017) as they provide a better estimation of element concentration in the sediments:

$$clr\ A = \ln\left(\frac{A}{Ag}\right)$$

Here, *clr A* represents the central log ratio, determined as the measurement of the element (*A*) by the geometric mean (*Ag*) of all the elements analysed. The central log ratios were subsequently used to produce a robust cluster analysis and evaluate the geochemical composition of the sediments without prior knowledge. Further information was derived from biplots of the clustering analyses, which helped to visualize the loadings (variables) of the principal component analyses (PCA) and estimate the best element associations to represent the cored sediments. Element ratios were plotted as log-normalized ratios [=ln(*A*/*B*)] after Weltje & Tjallingii (2008).

Element ratios of ln (Zr/Rb) were used to discriminate grain-size changes in deep-water sediments (Wu *et al.*, 2020), whereas ln (Ca/Ti) indicates variations in the biogenic (Ca) and detrital (Ti) input, if the sediments contain calcareous microfossils (Vandorpe *et al.*, 2019), such as the studied cores (Villa *et al.*, 2003; Hillenbrand *et al.*, 2021). In addition, ln (Ba/Al) was used as an established reliable palaeoproductivity proxy for Antarctic continental margin sediments (e.g. Hillenbrand *et al.*, 2021, and references herein), while ln (Fe/Ti) and ln (Mn/Al) were used to characterize the redox conditions in the sediment column and, thus, infer the oxygenation of pore and palaeo-bottom waters (Spofforth *et al.*, 2008; Vandorpe *et al.*, 2019). The XRF data, cluster analyses and PCA are openly available in the Mendeley Data Repository, at: http://doi.org/10.17632/524cr43x9j.1.

Grain-size analysis

Samples for grain-size analyses were collected every 10 cm for the whole length of cores SEDANO 12 and 13, and every 20 cm for cores SEDANO 11, 18 and 20. The JR298 cores were sampled at 10 to 20 cm intervals. In total, 317 samples were collected to study the textural properties of the sediments.

Grain-size analyses were prepared and carried out in 2019 and 2020 at the University of Bordeaux, France. Initially, bulk sediment samples were dried at 40°C for 24 h to determine their total dry weight. Dry sieving over 2 mm was conducted for samples with grains too coarse for laser particle-size analysis. About 1 to 2 g of sediment was collected for laser grain-size analysis and treated by three different procedures to remove the biogenic components, i.e. calcium carbonate ($CaCO_3$), organic matter and biogenic silica. The samples were initially decalcified in a hydrochloric acid (HCl) 37% solution, resuspended in distilled water, and dried in an oven at 40°C. After this procedure, the organic matter was removed by submersion of the sample in a hydrogen peroxide (H_2O_2) 35% solution. The resulting sample was resuspended in distilled water (H_2O) and dried in the oven at 40°C. The final procedure applied leaching with sodium carbonate (Na_2CO_3) 2 M solution in a bain-marie at 90°C, followed by resuspension in distilled H_2O and drying at 40°C to remove the biogenic silica.

Grain-size analyses were performed on the treated samples using a laser microgranulometer Malvern Mastersizer hydro2000G with a size range of 0.020 to 2000 μm (Malvern Panalytical, Malvern, UK). The grain-size distribution was analysed using the GRADISTAT software (Blott & Pye, 2001), which plots the grain-size results across histograms, logarithmic plots and ternary diagrams, according to the geometric graphical methods of Folk & Ward (1957) to assess the clay, silt and sand content. Sorting, skewness and kurtosis are described using the scheme proposed by Folk & Ward (1957) and mean grain size uses a modified Udden-Wenthworth grade scale (Blott & Pye, 2001). Sortable silt (10 to 63 μm) mean size ($\overline{SS}$) and sortable silt percentage (SS%) within the fine fraction (<63 μm) were calculated following the methods of McCave *et al.* (1995, 2017) and McCave & Andrews (2019). Using the Weddell/Scotia Sea calibration equation from table 2 in McCave *et al.* (2017), scalar flow speed (cm s^{-1}) was calculated from measured $\overline{SS}$ to estimate the palaeocurrent speed of the bottom current:

$$U = \frac{\overline{SS} - 12.73}{0.515}$$

where U is scalar flow (cm s^{-1}) and $\overline{SS}$ represents the mean sortable silt (McCave *et al.*, 2017).

Thin sections

Samples for thin sections were collected every 20 to 50 cm as 2 × 3 cm cubes in the SEDANO-II cores, adjacent to grain-size

© 2022 The Authors. *Sedimentology* published by John Wiley & Sons Ltd on behalf of International Association of Sedimentologists, *Sedimentology*, **69**, 1953–1991

samples, or when changes in sedimentary facies were observed. Sampling also focused on sand-rich or coarse silt beds. The samples were cut and ground smooth to 30 μm thickness at the Royal Holloway University of London, United Kingdom, following standard soft sediment impregnation methods (Palmer *et al.*, 2008; Meer & Menzies, 2011; Menzies & van der Meer, 2018). In total, 84 normal thin sections and 76 dyed sections were produced to examine the microfacies under a polarizing petrographic microscope.

Ichnological analysis

Ichnological analysis was conducted after digital enhancement of the high-resolution core photographs to enhance visibility of the biogenic structures. Their identification followed the procedures described in Dorador *et al.* (2014a, 2014b), Dorador & Rodríguez-Tovar (2018) and Miguez-Salas *et al.* (2019). Ichnological features such as orientation, shape, size, distribution, infilling material and degree of bioturbation were recorded, allowing ichnotaxonomical classification (Knaust, 2017).

Age models

High-resolution age models had been previously established for several SEDANO cores (including SED-12 and SED-13) and all of the JR298 piston cores by applying relative palaeointensity (RPI) dating (Sagnotti *et al.*, 2001; Macrì *et al.*, 2006; Venuti *et al.*, 2011; Channell *et al.*, 2019). Based on those age constraints, sedimentation rates were calculated for cores PC728, PC736, SED-12 and SED-13 (Table 2). For cores without RPI age models (SED-11, SED-18 and SED-20), previously published age models were used based on proxy correlations constrained by biostratigraphy, RPI-dating and tephrochronology (Lucchi *et al.*, 2002; Villa *et al.*, 2003; Hillenbrand *et al.*, 2008b, 2021; Venuti *et al.*, 2011). Figure S3 and Table S1 provide the chronostratigraphic constraints for the sediment cores.

Nomenclature

This study follows the criteria proposed by Stow & Tabrez (1998) for the identification and description of hemipelagic deposits. The classification of fine to coarse-grained contourites follows the nomenclature proposed by Faugères & Stow (2008) and Rebesco *et al.* (2014), as well as the textural classification of Brackenridge *et al.* (2018). The description of fine to coarse-grained turbidites is based on Middleton & Hampton

Table 2. Sedimentation rates (cm kyr^{-1}) for cores PC728, PC736, SED-12 and SED-13 based on the age models of Macrì *et al.* (2006), Venuti *et al.* (2011) and Channell *et al.* (2019). Main sedimentary facies across each interval based on the detailed core descriptions of Fig. S1.

PC728					PC736					SED-12					SED-13				
Main facies	Depth (cm)	Age (ka)	Thickness (cm)	Sed. rate (cm kyr^{-1})	Main facies	Depth (cm)	Age (ka)	Thickness (cm)	Sed. rate (cm kyr^{-1})	Main facies	Depth (cm)	Age (ka)	Thickness (cm)	Sed. rate (cm kyr^{-1})	Main facies	Depth (cm)	Age (ka)	Thickness (cm)	Sed. rate (cm kyr^{-1})
–	0	0	–	–	–	0	0	–	–	–	0	0	–	–	–	0	0	–	–
b	35	4.44	35	7.88	b/a	66	8.75	66	7.54	g/a	50	9.62	50	5.20	a	50	5.04	50	9.92
a	58	8.33	23	5.91	d/a	113	13.60	47	9.69	a/g	104	17.24	54	7.09	a/g	100	9.71	50	10.71
e	132	13.61	74	14.02	a/d	160	16.52	47	16.16	a/g	150	20.59	46	13.73	a/g	150	15.41	50	8.77
e/a	397	22.22	265	30.78	d/a	283	26.00	123	12.97	g/a	200	27.89	50	6.85	a/g	200	19.35	50	12.69
e/a	412	26.66	15	3.38	d	486	32.86	203	29.59	g/a	250	31.90	50	12.47	a/g	250	27.09	50	6.46
a	443	29.44	31	11.15	b/a/e	600	41.00	114	14.00	a/g	300	35.13	50	15.48	a/g	300	31.81	50	10.59
a	486	39.72	43	4.18	a/e	643	46.78	43	7.44	g/a	350	38.56	50	14.58	a	350	35.89	50	12.25
a	556	44.16	70	15.76	e/a	900	63.77	257	15.13	g/a	400	43.28	50	10.59	a/g	400	40.90	50	9.98
a/e	665	50.27	109	17.84	c/a	983	71.55	83	10.67	a/g	450	48.43	50	9.71	a/g	450	47.84	50	7.20
e/a	727	58.05	62	7.97						a/g	500	51.65	50	15.53	a/g	500	55.17	50	6.82
a/e	836	63.88	109	18.70						a/g	550	58.16	50	7.68	a/g	553	61.41	53	8.49
a/e	968	69.44	132	23.74						a	600	64.67	50	7.68	a	600	68.3	47	6.82
a	991	77.78	23	2.76						a/g	650	71.55	50	7.27	a/g	650	74.44	50	8.14
a	1082	94.72	90	5.31						a/g	690	76.55	40	8.00	a/g	662	75.92	12	8.11
a	1120	99.16	39	8.78															

© 2022 The Authors. *Sedimentology* published by John Wiley & Sons Ltd on behalf of International Association of Sedimentologists, *Sedimentology*, **69**, 1953–1991

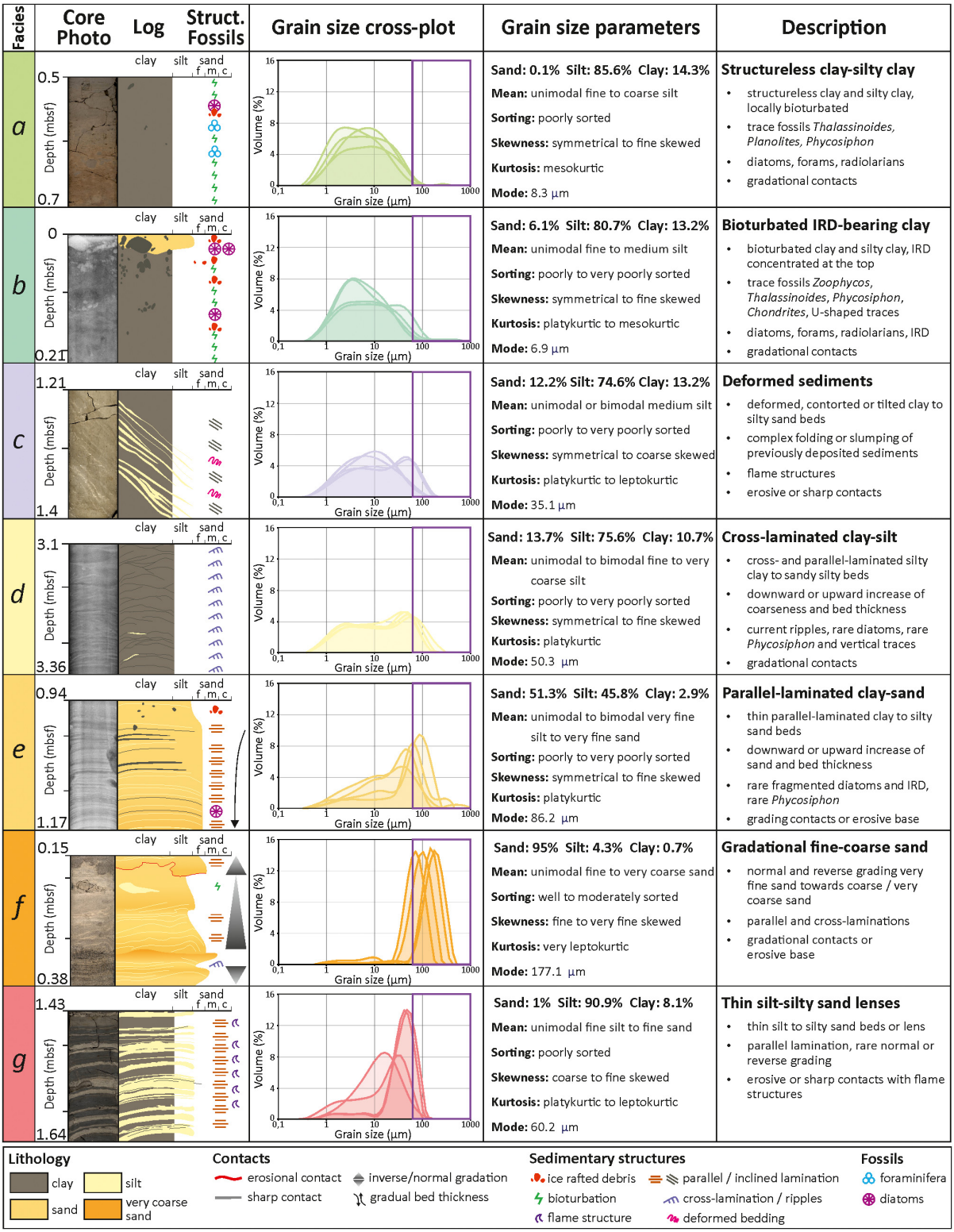

Fig. 4. Summary of the seven sedimentary facies ('a' to 'g') identified in this study, complemented by core photographs, X-radiographs, core logs and grain-size parameters. The grain-size distribution plots and statistical grain-size data present the average measurements for each facies. The purple box in the grain-size distribution plots highlights the sand fraction from 63 to 1000 µm.

© 2022 The Authors. *Sedimentology* published by John Wiley & Sons Ltd on behalf of International Association of Sedimentologists, *Sedimentology*, **69**, 1953–1991

(1973), Lowe (1982) and Stow & Piper (1984). The identification of gradual or transitional facies is based on the concepts proposed by Shanmugam *et al.* (1993), de Castro *et al.* (2020, 2021) and Fonnesu *et al.* (2020).

RESULTS

Sedimentary facies

Seven sedimentary facies have been identified throughout the sediment cores (Figs 3 and S2). The full lithological description and facies interpretation for each sediment core, along with X-radiographs for the JR298 cores and core photographs for the SEDANO cores, are included in Fig. S2.

Facies-a: structureless clay and silty clay

Facies-a consists of structureless (or very faintly laminated) clay and diatom-bearing silty clay of predominantly grey-brown to brown or olive-brown colour, with gradational tops and bases (Fig. 3A). Locally, this facies can appear bioturbated; certain intervals have a mottled texture, while others show clear, discrete traces of *Thalassinoides* and *Planolites* (Fig. 3A). Its sediment may contain diatoms, foraminifera and radiolarians (Fig. 3, section '1'). The intervals with faint laminations may be occasionally disrupted by very small traces of *Phycosiphon* (Fig. 3C). In general, the thickness of this facies varies between 5 cm and up to 3 m (Fig. 2). Facies-a represents *ca* 40 to 50% of the total sediment thickness in most cores (Fig. S2).

Textural analyses indicate that Facies-a comprises unimodal fine to coarse silt (with a mode of *ca* 8.3 μm; Figs 4, 5 and 6A), that is poorly sorted ('*trend a* and *b*' in Fig. 7A and B and following '*trend a* and *b*' in Fig. 8), with a symmetric to fine skewed mesokurtic distribution (between '*trend a* and *b*' in Fig. 7D). Facies-a has a $\overline{SS}$ of 20 μm (between 14 μm and 33 μm) and a relatively variable SS% of 34% (between 11% and 62%; Fig. 12). It has high ln (Fe/Ti) and occasionally high ln (Mn/Al) and ln (Ba/Al; Fig. 9A), and low ln (Ca/Ti) and ln (Zr/Rb). Yet, these ratios are higher at transitions to other facies (Fig. 9).

Facies-b: bioturbated and ice-rafted debris-bearing clay and silty clay

Facies-b is defined as intensely bioturbated clay and silty clay (Fig. 3A) with coarse-grained ice-rafted debris (IRD). The bioturbated clay and silty clay is dark greyish-brown or brown, and the IRD ranges in colour from black to dark brown. The IRD clasts are angular and appear to be more concentrated towards the top of Facies-b (Fig. 3A). This facies is characterized by gradual top and basal contacts (Fig. 6A). Facies-b is also characterized by the highest abundance of trace fossils and ichnodiversity. Discrete trace fossils mainly consisting of *Zoophycos*, *Thalassinoides* and *Planolites*, with occasional *Chondrites* and U-shaped structures, are superimposed on a mottled background texture (Fig. 3A). Cross-cutting relationships between trace fossils are frequent (Fig. 3A). The matrix of Facies-b contains fragmented or whole diatoms, planktonic foraminifera and rare radiolarians (Fig. 3, section '1'). In most of the cores, Facies-b is usually present near the core tops (Fig. S2).

Facies-b is characterized by unimodal fine to medium silt (with a mode of *ca* 6.9 μm; Figs 4 and 5), poorly to very poorly sorted ('*trend a*' in Figs 7A, 7B and 8), with a symmetrical to fine skewed mesokurtic to platykurtic trend ('*trend a*' in Fig. 7A to D). The sortable silt data of Facies-b are similar to those of Facies-a, with $\overline{SS}$ being on average 20 μm (between 16 μm and 24 μm) and SS% being 34% (22 to 43%; Fig. 12). The bioturbated clay and silty clay beds show high ln (Fe/Ti) and ln (Ba/Al) and low ln (Ca/Ti) and ln (Zr/Rb). The top of Facies-b, which is enriched in IRD, is characterized by low ln (Ba/Al) and ln (Fe/Ti), and high ln (Zr/Rb).

Facies-c: deformed sediments

Facies-c is defined as contorted, tilted or deformed alternating clay to silty sand beds (Fig. 4), representing complex folding and slumping of previously deposited sediments (from Facies-a to Facies-g), with steeply dipping layers (Fig. 3D). The clays and silty clays are dark brown or dark grey-brown, while the interbedded clayey silts and muddy sands are light to dark yellow (Fig. 3D). Angular IRD and fragmented, soft-sediment clasts are dispersed throughout the sediments. Trace fossils are absent. Base and top contacts are usually erosive or sharp (Fig. 3M). Facies-c exhibits deformed parallel-laminations and occasional flame structures across the top and basal contacts. This facies appears abundantly along the steep south-west drift flanks and submarine channels (Fig. 5) and occurs more rarely on the gently dipping north-east flanks and drift crests (Fig. S2).

© 2022 The Authors. *Sedimentology* published by John Wiley & Sons Ltd on behalf of International Association of Sedimentologists, *Sedimentology*, **69**, 1953–1991

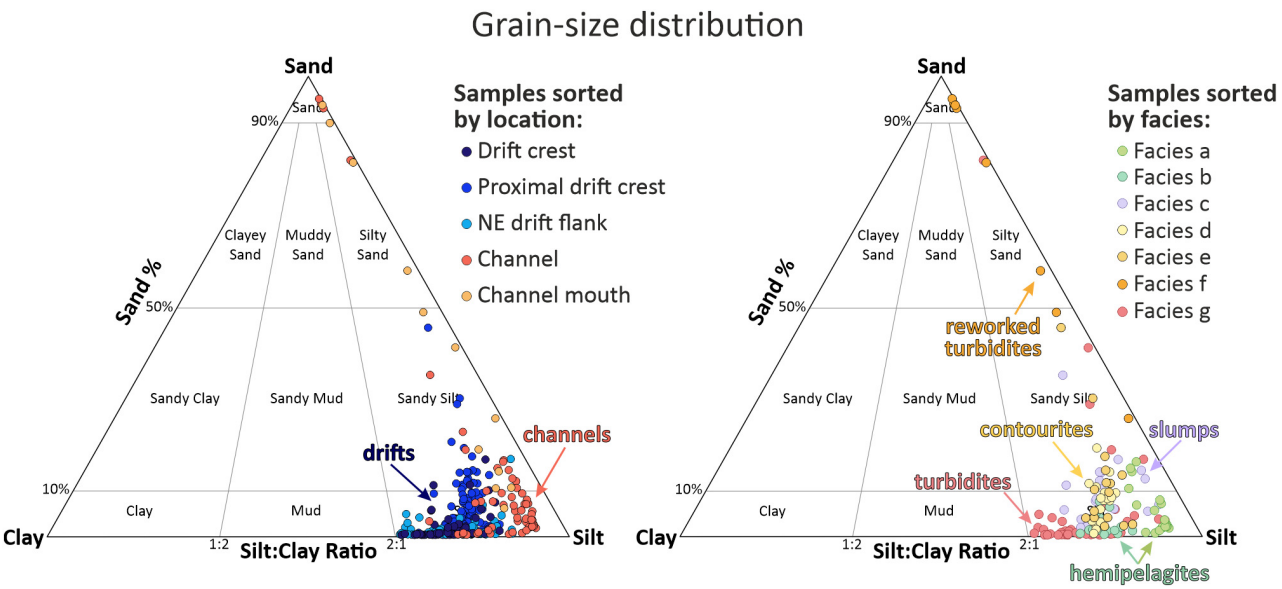

Fig. 5. Ternary plots for the percentages (%) of clay, silt and sand content. Drift facies (Facies-d and e) have high silt and sandy silt contents, while channel facies (Facies-g) trend from silt (silt : clay ratio >2 : 1) to sand (>90%). Depths of discrete grain-size samples are marked in Fig. S2.

Grain-size parameters for Facies-c show unimodal or bimodal medium silt (with a mode of *ca* 35.1 μm; Figs 4 and 5), which is poorly to very poorly sorted (between '*trend a* and *b*' in Fig. 7A and '*trend a* and *b*' in Fig. 8) and has a symmetrical to coarse skewed ('*trend a*' in Fig. 7B), platykurtic to leptokurtic population ('*trend b*' in Fig. 7D). Element ratios are usually low but can show spikes in the interbedded muddy sand beds (Fig. 10).

Facies-d: cross to parallel-laminated fine to coarse silt

Facies-d consists of repetitive sequences of cross to parallel-laminated fine to coarse silt laminae between 1 cm and 5 cm thick, grading upward into silty clay and clay (Fig. 3B). The silt laminae appear darkish yellow or olive to grey-brown; the silty clay and clay are dark brown or dark greyish brown. The base and top contacts correspond to gradational or slightly erosive contacts. Internal structures include transitions between cross-lamination, ripples, starving ripples and irregular wavy laminations (Fig. 3E). Rare IRD pebbles occur dispersed throughout Facies-d. The silt laminae have an argillaceous matrix with abundant quartz, feldspars and lithic clasts (of igneous or sedimentary origin), and more rarely fragmented bioclasts, biotite and exsolved iron-oxide particles (Figs 3 and 4). Bioturbation is scarce, with very small traces of *Phycosiphon* and the occasional record of vertical traces (Fig. 3B). A mottled bioturbated texture appears at the transition towards Facies-a or Facies-b. Facies-d is more abundant within the proximal drift crests and towards the gently dipping north-east flanks (Figs 5 and S2).

Textural analyses define Facies-d as unimodal to bimodal fine to very coarse silt (with a mode of *ca* 50.3 μm; Figs 4 and 6B), which is poorly to very poorly sorted ('*trend a*' in Figs 7A and 8) and has a symmetrical to fine skewed, platykurtic trend ('*trend a*' in Fig. 7D). Facies-d has an average $\overline{SS}$ of 25 μm (between 19 μm and 28 μm) and average SS% of 42% (between 19% and 52%) (Fig. 12). This facies presents highly variable values for all element ratios (Fig. 9A).

Facies-e: parallel-laminated clay to silty sand

Facies-e is defined by repetitive sequences of parallel-laminated clay to silty sand beds, which grade upward into silty clay and clay (Fig. 3F). The silt and silty sand are darkish yellow or olive to greyish brown, while the clay appears dark brown or dark grey-brown. Occasionally, grain size and bed thickness show a general increase with depth from 1 to 10 cm thick beds with gradational contacts (Fig. 3C). The thickest sand beds (*ca* 10 cm) are massive (Fig. 6A). The base and top contacts are gradational or, less

© 2022 The Authors. *Sedimentology* published by John Wiley & Sons Ltd on behalf of International Association of Sedimentologists, *Sedimentology*, **69**, 1953–1991

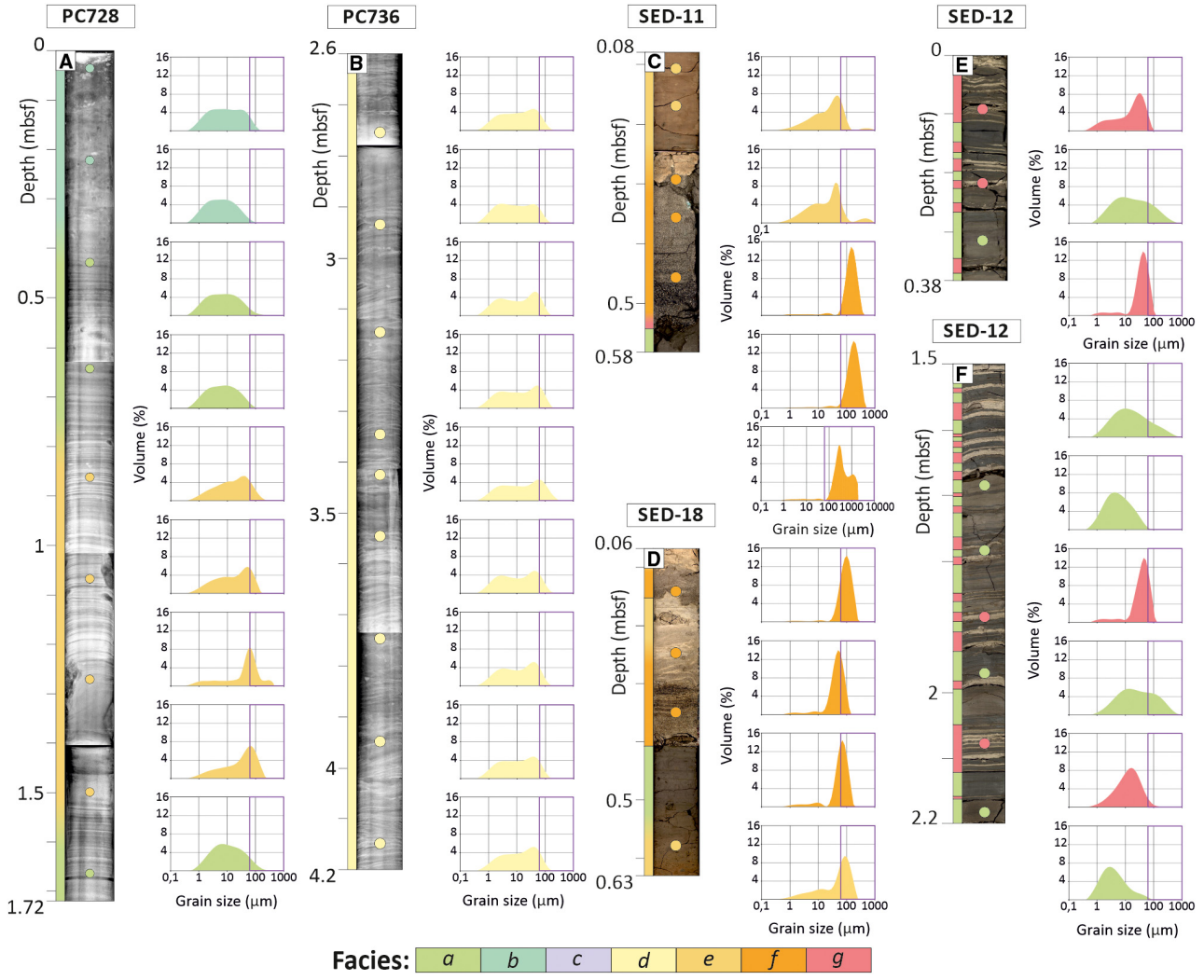

Fig. 6. High-resolution core images, X-radiographs and grain-size distributions for the main sedimentary facies ('a' to 'g'). The coloured dots on the photographs/X-radiographs mark the depths of the discrete grain-size samples. The purple box in the grain-size distribution plots highlights the sand fraction from 63 to 1000 µm. Depth ranges of core intervals are given in Fig. 2.

frequently, sharp (Fig. 6A). Bioturbation is rare, with the occasional record of very small traces of *Phycosiphon* within fine-grained horizons (Fig. 3C). The matrix of the silt to sand beds is characterized by rare argillaceous material with sub-angular to round quartz, feldspars and volcaniclastics, and rare fragmented bioclasts, biotite and exsolved iron-oxides (Fig. 3, sections '2' and '3'). Facies-e is more abundant at the proximal drift crests (Figs 5 and S2).

Grain-size parameters indicate that Facies-e corresponds to unimodal to bimodal very fine silt to very fine sand (with a mode of *ca* 86.2 µm; Figs 4 and 5), poorly to very poorly sorted ('*trend a*' in Figs 7A, 7B and 8), with a symmetrical to fine skew and platykurtic trend ('*trend a*' in Fig. 7C and D). It has relatively high average $\overline{SS}$ of 24 µm (17 to 36 µm) and average SS% is 43% (23 to 73%; Fig. 12). Facies-e is characterized by high ln (Zr/Rb) while the other elemental ratios are low (Fig. 9A).

Facies-f: cross-laminated fine to very coarse sand

Facies-f is characterized by coarse beds of very fine or medium sand to coarse or very coarse sand and gravel (Fig. 3I and K). The fine to medium sands are very dark brown or yellowish brown at the base and coarsen upward into very coarse dark brown sand before fining upward

© 2022 The Authors. *Sedimentology* published by John Wiley & Sons Ltd on behalf of International Association of Sedimentologists, *Sedimentology*, **69**, 1953–1991

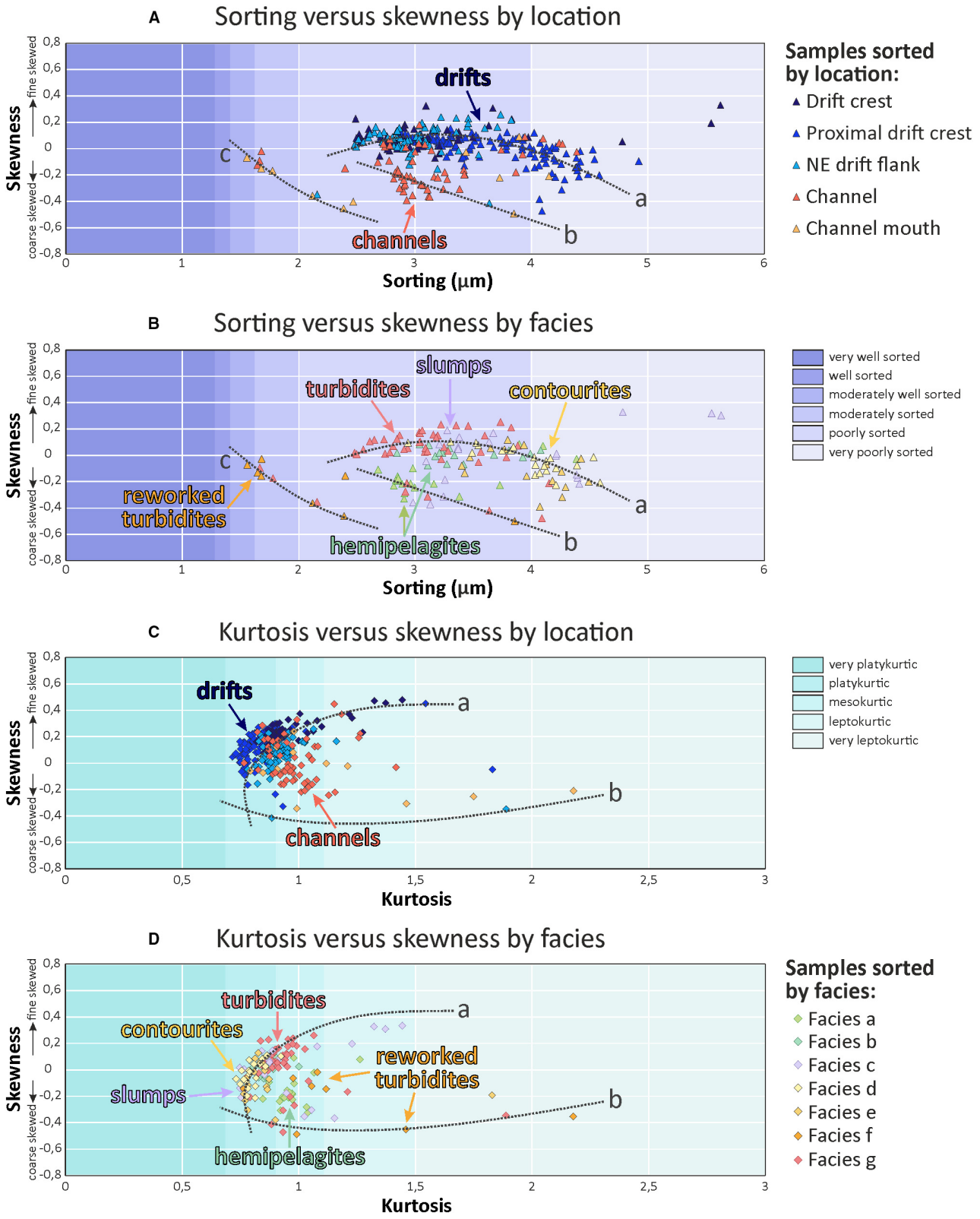

Fig. 7. Cross-plots of sorting versus skewness (A and B), and skewness versus kurtosis (C and D) for sediment samples distinguished by location and by facies, respectively; lines a, b and c indicate logarithmic trends. Depths of discrete grain-size samples are marked in Fig. S2.

© 2022 The Authors. *Sedimentology* published by John Wiley & Sons Ltd on behalf of International Association of Sedimentologists, *Sedimentology*, **69**, 1953–1991

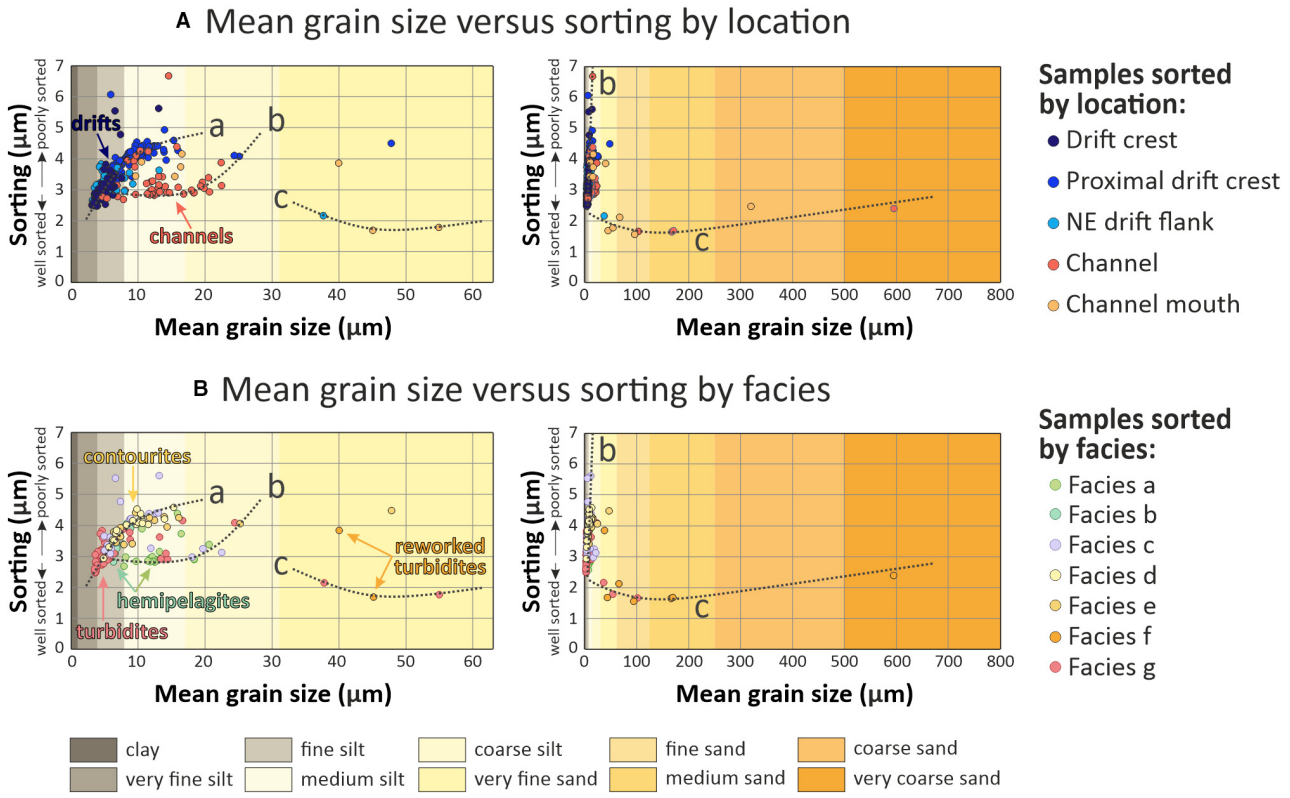

Fig. 8. Cross-plots of mean grain size versus sorting distinguished by location (A) and by facies (B); lines a, b and c indicate logarithmic trends. Depths of discrete grain size samples are marked in Fig. S2.

towards greyish brown or light beige medium to fine sand (Fig. 4). Their thickness ranges between 10 cm and 30 cm. Base and top contacts with other facies are gradational or erosional (Fig. 3I and K). The sand intervals are characterized by sub-angular to round quartz, feldspars, altered volcaniclastics and rare bioclast fragments, biotite, and exsolved iron-oxides (Fig. 3, sections '2' and '3'). This facies is characterized by the presence of cross-laminations and parallel-laminations (Fig. 3I and K). Granules are tightly concentrated and oriented along the lamination trend of the coarsest sand beds (Fig. 3I) with pebbles observed across erosional bases (Fig. 3I and K). Coarse sand infilled traces were not observed across the coarse sand intervals of Facies-f nor in the underlying facies (Fig. 3I). Facies-f commonly occurs on the distal parts of the mounded drifts, near or within the trunk channels (Figs 5 and S2).

According to grain-size measurements, Facies-f comprises unimodal fine to very coarse sand (with a mode of *ca* 177.1 μm; Figs 4, 6C and 6D) that is well to moderately sorted ('*trend c*' and secondarily '*b*' in Fig. 7B and along '*trend c*' in Fig. 8), with a symmetrical to very fine skewed trend and a very leptokurtic distribution (along '*trend b*' and distributed towards '*trend a*' in Fig. 7D). It has high values for $\overline{SS}$ and SS%, on average 36 μm (between 26 μm and 49 μm) and 72% (between 49 μm and 94 μm) (Fig. 12). Facies-f is characterized by increasing ln (Zr/Rb) values from the base to the centre of the facies, where it inverts and decreases towards the top (Fig. 9A). Ln (Mn/Al), ln (Ba/Al) and ln (Fe/Ti) ratios show the opposite trend, with higher values near the base that decrease towards the centre and increase towards the top (Fig. 9A). Spikes in ln (Zr/Rb) mark the coarser-grained beds (Fig. 9A).

Facies-g: thin silt and silty sand lenses

Facies-g consists of yellowish and on average 1 to 3 cm thick (up to 5 cm thick) interbedded silt or silty sand lenses or laminae (Fig. 3J and L). Internal grain-size variations are rare, with either reverse or normal grading between silty clay and silty sand (Fig. 3G). The base and top

© 2022 The Authors. *Sedimentology* published by John Wiley & Sons Ltd on behalf of International Association of Sedimentologists, *Sedimentology*, **69**, 1953–1991

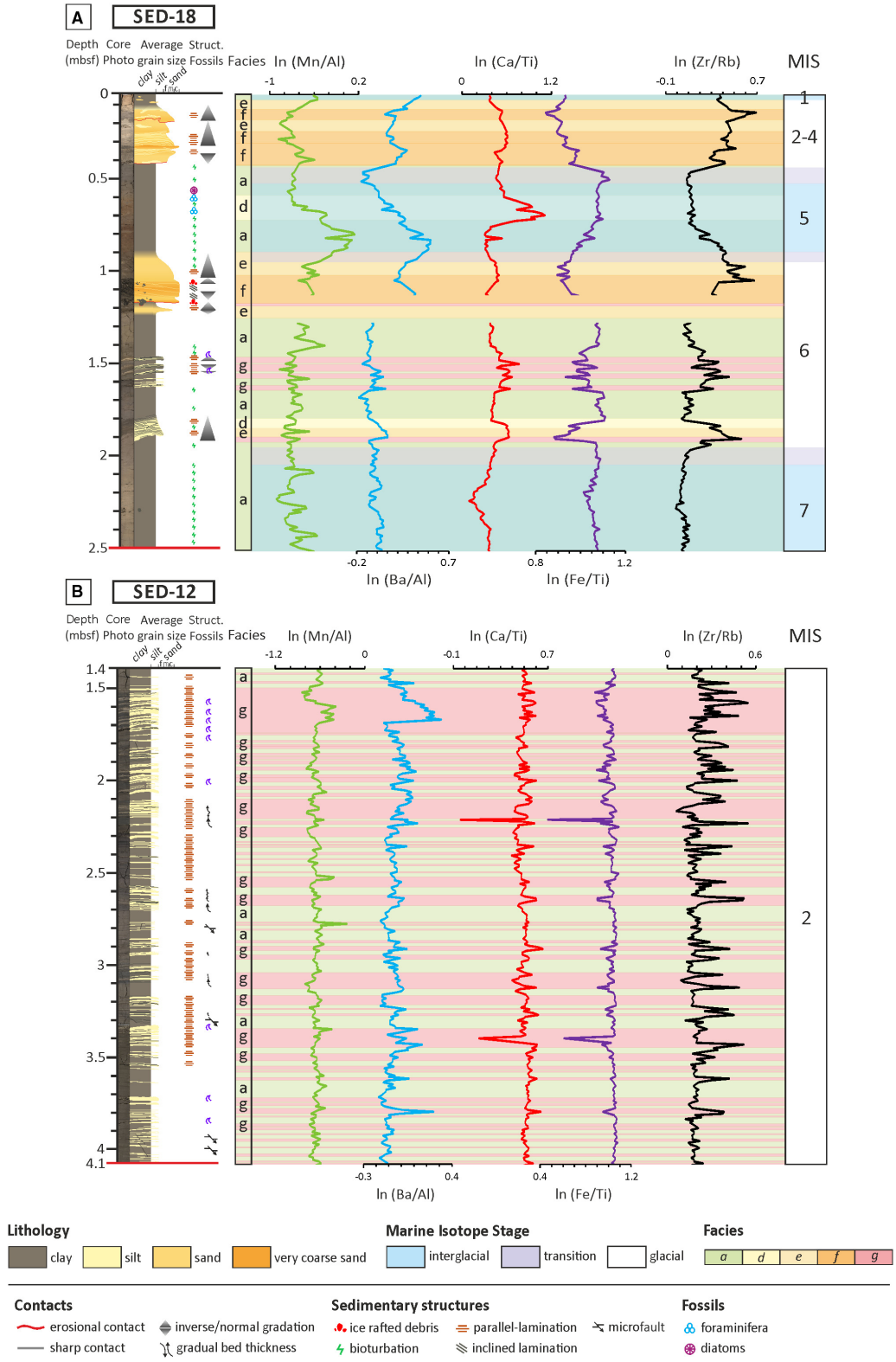

Fig. 9. Lithological logs, X-ray fluorescence (XRF) scanner data and assigned Marine Isotope Stage (MIS) for sediment cores SED-18 (A) and SED-12 (B), from left to right: ln (Mn/Al), ln (Ba/Al), ln (Ca/Ti), ln (Fe/Ti) and ln (Zr/Rb). MIS after Lucchi *et al.* (2002).

© 2022 The Authors. *Sedimentology* published by John Wiley & Sons Ltd on behalf of International Association of Sedimentologists, *Sedimentology*, **69**, 1953–1991

contacts are erosive with frequent flame structures (Fig. 3, section '5'), or rip-up clasts at the base. The silt to silty sand laminae are interbedded by argillaceous brown to dark brown matrix (Fig. 3, section '4'), while the sand-grains consist mainly of quartz, feldspars, rare lithic or bioclast fragments, and exsolved iron-oxides (Fig. 3, section '6'). Facies-g exhibits parallel-laminations or rare concave or contorted beds, which follow the same orientation as the flame structures. It is also characterized by normal or reverse microfaults (Fig. S2.2). Facies-g is more abundant within channels and along the edges of the drift flanks near the channels (Figs 5 and S2).

Textural analyses characterize Facies-g as unimodal fine silt to fine sand (with a mode of *ca* 60.2 μm; Figs 5, 6E and 6F), which is poorly sorted (Figs 7B and 8) and has a coarse to fine skewed grain population ('*trend a*' mainly, '*trends b* and *c*' secondarily in Fig. 7B) with a platykurtic to leptokurtic trend ('*trend a*' mainly and dispersed towards '*trend b*' on Fig. 7D). This facies is characterized by generally high values for all element ratios, except for ln (Fe/Ti; Fig. 9B).

DISCUSSION

Reconstruction of depositional processes and paleoenvironmental conditions

Hemipelagic deposits/very fine-grained contourites (Facies-a and b)

The structureless clay to silty clay of Facies-a and the bioturbated, IRD-bearing clay and silty clay of Facies-b are interpreted as hemipelagites or very fine-grained contourites (Fig. 4). The high clay and silt content along with high ln (Fe/Ti) suggests subtle fluctuations in sediment supply or in the hydrodynamic regime (Figs 5 and 6A). Trace fossil assemblages, if present, consist mainly of *Zoophycos*, *Thalassinoides* and *Planolites* (Fig. 3A) and can be assigned to the *Zoophycos* ichnofacies, usually related to fine-grained pelagic and hemipelagic sediments (e.g. Rodríguez-Tovar *et al.*, 2015a, 2015b, 2020). The bioturbation and cross-cutting relationships between *Zoophycos*, *Thalassinoides* and *Planolites* over a mottled background texture of Facies-b (Fig. 3A) reveal a well-developed multitiered tracemaker community, associated with favourable palaeoenvironmental conditions, such as oxygenation and food availability (Hodell *et al.*, 2017; Rodríguez-Tovar *et al.*, 2019, 2020). Ichnological data, along with peaks in ln (Mn/Al) and ln (Ca/Ti), suggest relatively high biological productivity (Fig. 9). The sedimentation rates calculated from the age models are generally low to moderate (2.76 to 7.88 cm kyr^{-1} for Facies-a and b in Table 2), offering enough time for biota to burrow the sediments (Lucchi *et al.*, 2002; Lucchi & Rebesco, 2007; Rodríguez-Tovar & Hernández-Molina, 2018). These facies present a platykurtic to mesokurtic distribution (Figs 6A and 7) and unimodal shape with a mode *ca* 7.5 μm (Fig. 4) that is characteristic of hemipelagic deposits (Brackenridge *et al.*, 2018; de Castro *et al.*, 2020, 2021). The relatively high input of IRD content in Facies-b (Fig. 3A) reflects free drift of icebergs across the continental margin, which can be associated with increased iceberg calving and/or reduced sea-ice cover. Therefore, the intervals of Facies-b and Facies-a with moderate to intense bioturbation, IRD, foraminifera and diatoms (Fig. 4) mark the establishment of interglacial conditions, as proposed in previous studies (Pudsey & Camerlenghi, 1998; Pudsey, 2000, 2002; Ó Cofaigh *et al.*, 2001; Lucchi *et al.*, 2002; Villa *et al.*, 2003; Lucchi & Rebesco, 2007). For intervals without bioturbation, IRD or foraminifera, the structureless to faintly laminated clay and silty clay was probably deposited during glacial periods (Fig. 11). Both $\overline{SS}$ and SS% are relatively low (Fig. 12), suggesting minor changes in bottom current speed (on average 8.7 cm s^{-1}, with a full range of 1 to 25 cm s^{-1} in Fig. 13) with a dominance of hemipelagic settling, which is in agreement with other studies on Late Quaternary sediments and recent bottom-current measurements (6.2 ± 3.4 cm s^{-1}; Camerlenghi *et al.*, 1997; Pudsey & Camerlenghi, 1998; Moerz & Wolf-Welling, 2001; Giorgetti *et al.*, 2003; Hillenbrand *et al.*, 2021). Various supply mechanisms could provide the fine-grained particles, such as suspension fallout from low-density turbidity currents and sediment-laden meltwater plumes, or pelagic settling of planktonic organisms (Barker *et al.*, 1999). As such, these mechanisms would form hemipelagic deposits or very fine-grained contourites (Fig. 3) if under the influence of a weak bottom current (Fig. 13).

Mud-rich contourites (Facies-d)

The cross-laminated to rippled clay and silt laminae of Facies-d may represent very fine-grained contourite deposits (Fig. 14), formed under the influence of persistent bottom currents (Stow *et al.*, 2009; Baas *et al.*, 2016). The mud ripple

© 2022 The Authors. *Sedimentology* published by John Wiley & Sons Ltd on behalf of International Association of Sedimentologists, *Sedimentology*, **69**, 1953–1991

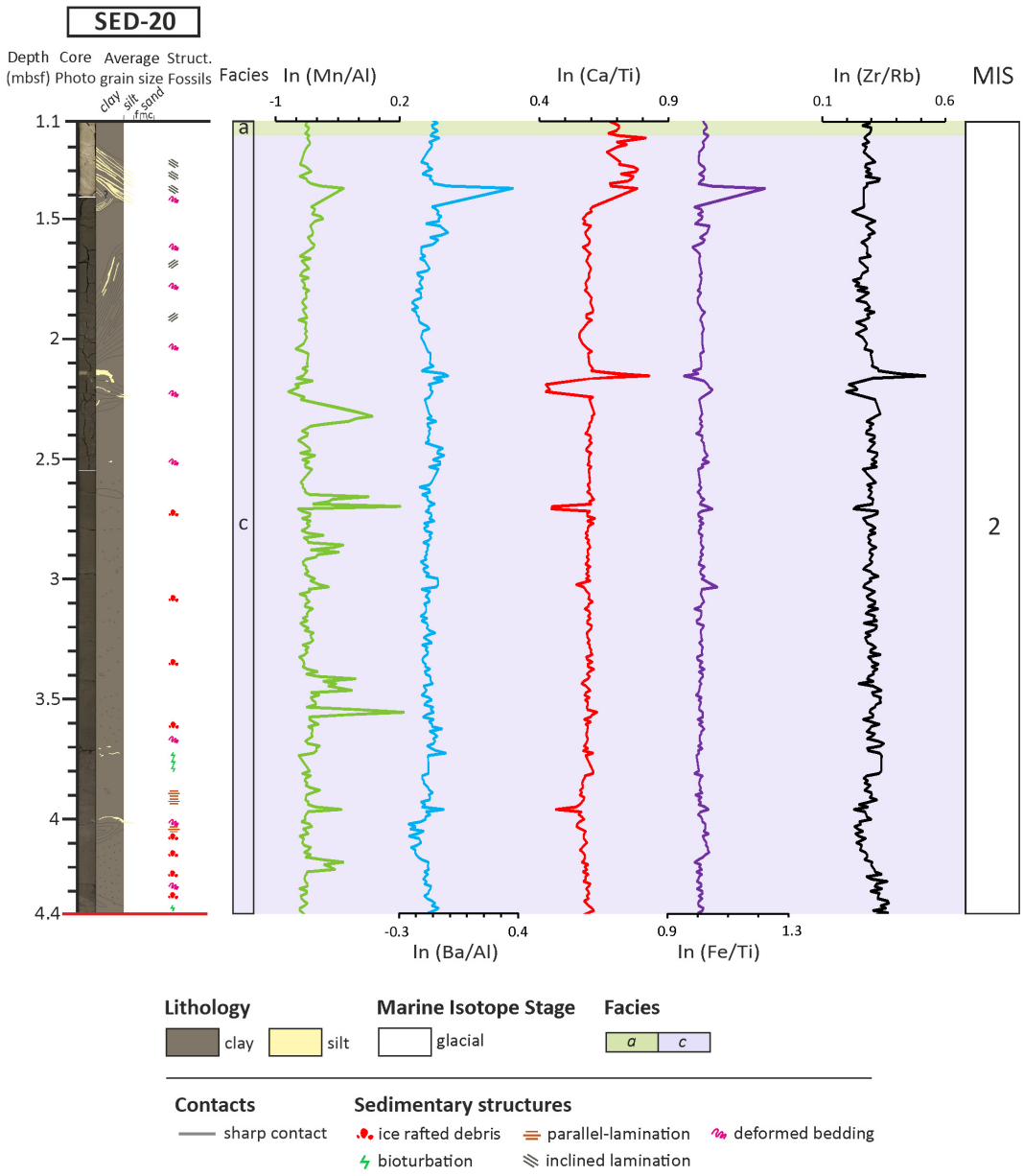

Fig. 10. Lithological log, X-ray fluorescence (XRF) scanner data and assigned Marine Isotope Stages (MIS) for sediment core SED-20, from left to right: ln (Mn/Al), ln (Ba/Al), ln (Ca/Ti), ln (Fe/Ti) and ln (Zr/Rb). MIS after Lucchi *et al.* (2002).

sequences (Fig. 3E) along with highly variable element ratios (Fig. 9A) reflect subtle, fluctuating current velocities. $\overline{SS}$ and SS% support this conclusion (Fig. 12), as they suggest bottom current speeds equal to or slightly higher than the modern average current velocities (on average 16.9 cm s^{-1}, with a full range of 5 to 24 cm s^{-1} in Fig. 13; McCave *et al.*, 2017). The platykurtic, symmetrical to fine skewed distribution (Figs 6B and 7), bimodal shape and mode of 50.3 μm (Fig. 4) suggest reworking and winnowing as the dominant processes involved in the deposition of these sediments (Brackenridge *et al.*, 2018), which were probably sourced by suspension fallout of low-density turbidity flows (Postma, 1986; Stanley, 1987, 1988, 1993; de Castro *et al.*, 2020, 2021). The scarce traces of *Phycosiphon* and the occasional record of vertical traces

© 2022 The Authors. *Sedimentology* published by John Wiley & Sons Ltd on behalf of International Association of Sedimentologists, *Sedimentology*, **69**, 1953–1991

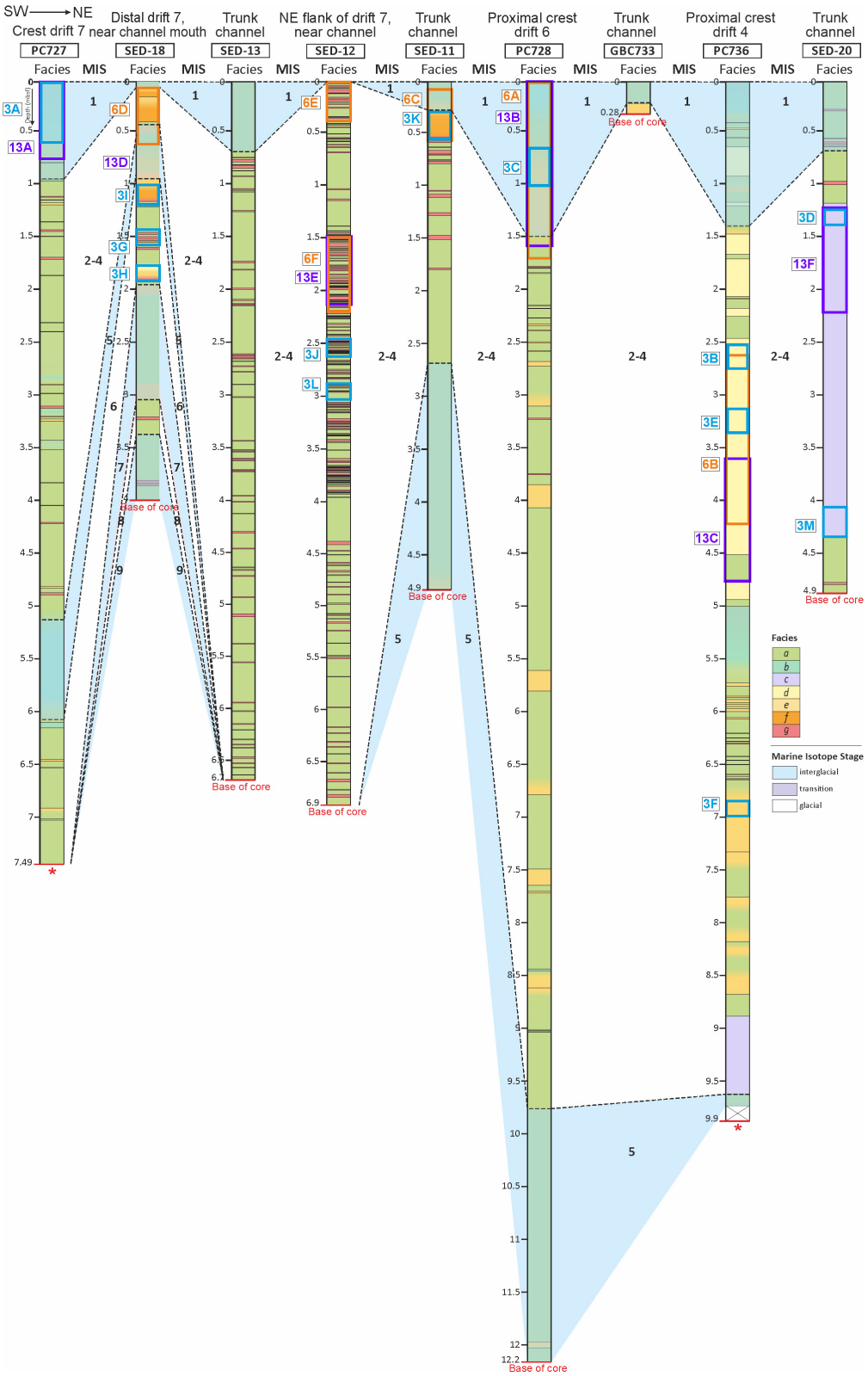

Fig. 11. Sedimentary facies and Marine Isotope Stages (MIS) for all studied cores. MIS of the SEDANO cores after Lucchi *et al.* (2002) and Lucchi & Rebesco (2007) and of the JR298 cores after Channell *et al.* (2019) and Hillenbrand *et al.* (2021). *: core interval disturbed by flow-in at the base (not shown).

© 2022 The Authors. *Sedimentology* published by John Wiley & Sons Ltd on behalf of International Association of Sedimentologists, *Sedimentology*, **69**, 1953–1991

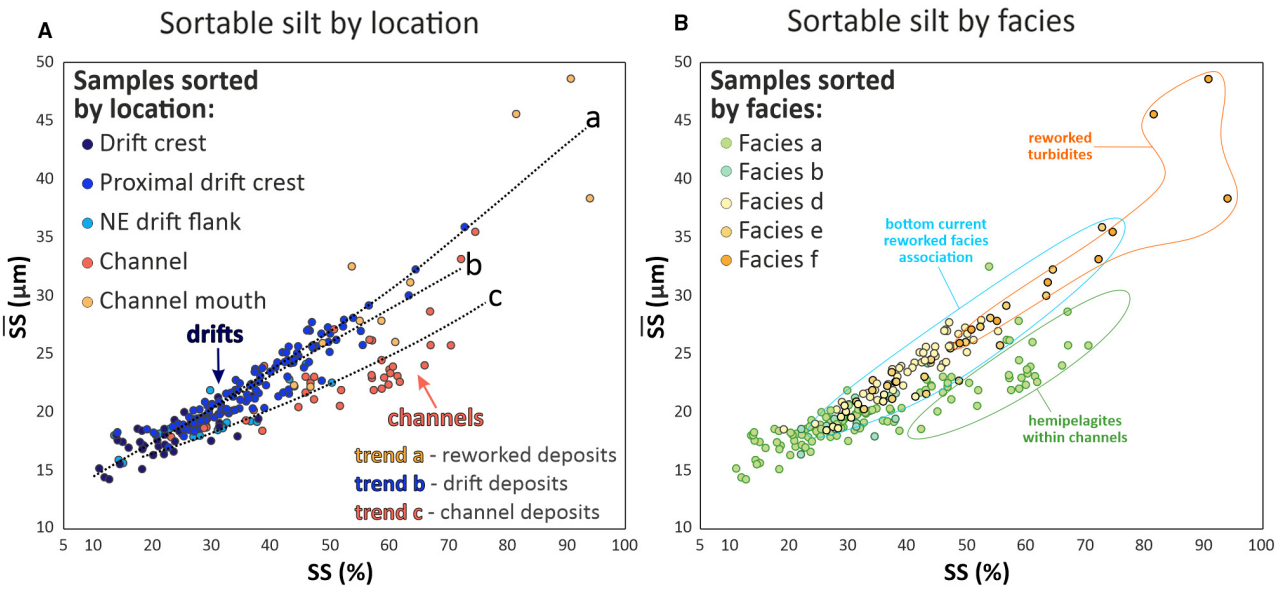

Fig. 12. Cross-plots of mean sortable silt ($\overline{SS}$) versus sortable silt percentage (SS%) distinguished by location (A) and by facies (B); lines a, b and c indicate linear and exponential trends. Depths of discrete grain size samples are given in Fig. S2.

across a few muddy beds (Fig. 3B) imply moderate to high sedimentation rates (9.69 to 29.59 cm kyr^{-1} in PC736; Table 2) and a relatively unfavourable environment for benthic organisms, with short periods of improved conditions (for example, higher food availability; Rodríguez-Tovar *et al.*, 2014). The occurrence of vertical traces could be diagnostic of episodic high sedimentation rates (Rodríguez-Tovar *et al.*, 2014). The presence of this facies along the gentle north-east drift flanks and towards the proximal crests (Fig. 5), with a highly variable ln (Zr/Rb; Fig. 9A), suggest that Facies-d may result from winnowing during or after the settling of fine-grained particles sourced by turbidity currents or meltwater plumes. This is consistent with previous sedimentological studies, which suggested that down-slope processes had delivered sediments to the deeper environments and filled a persistent nepheloid layer that was later redistributed by a steady bottom current (Rebesco *et al.*, 1996; Pudsey & Camerlenghi, 1998; Ó Cofaigh *et al.*, 2001; Lucchi *et al.*, 2002; Lucchi & Rebesco, 2007).

Sand-rich contourites (Facies-e)

The gradational contacts and fining upward of the parallel-laminated, silty sand facies (Figs 3C and 6A) are interpreted as a gradual transition in depositional conditions, supporting the formation of fine-grained sand-rich contourites instead of episodic turbidity currents, which would have erosional or sharp basal contacts (Gonthier *et al.*, 1984; Mutti, 1992; Faugères & Stow, 2008; de Castro *et al.*, 2020; Hüneke *et al.*, 2020). The upward decrease of bed thickness (Fig. 3C), sand content (Fig. 6A) and variable element ratios (Fig. 9A) represent fluctuating sediment supply or a variable hydrodynamic regime. The parallel-laminations along with a platykurtic, symmetrical to fine skewed distribution (Fig. 7) imply contouritic deposition, where the carrying capacity of the current is the limiting factor (Brackenridge *et al.*, 2018). Furthermore, the bimodal grain-size distribution (Figs 4 and 6A) is not a typical feature of turbidites, as these usually display a unimodal grain-size curve (Gong *et al.*, 2016). The dominance of lamination and the scarce presence of bioturbation, with small *Phycosiphon* (Fig. 3C), differ from typical contourite deposits (Gonthier *et al.*, 1984). The lithological variations of this facies (Figs 5 to 8), i.e. the parallel-laminated sandy beds, rare bioturbation and relatively scarce occurrence of IRD suggest that its deposition occurred during a glacial stage under high sedimentation rates (up to 30.78 cm kyr^{-1} in PC728; Table 2). The local presence of *Phycosiphon* could be associated with episodic pulses of abundant food supply (Rodríguez-Tovar *et al.*, 2014). The $\overline{SS}$ versus SS% trend (Fig. 12) suggests bottom current speeds occasionally higher

© 2022 The Authors. *Sedimentology* published by John Wiley & Sons Ltd on behalf of International Association of Sedimentologists, *Sedimentology*, **69**, 1953–1991

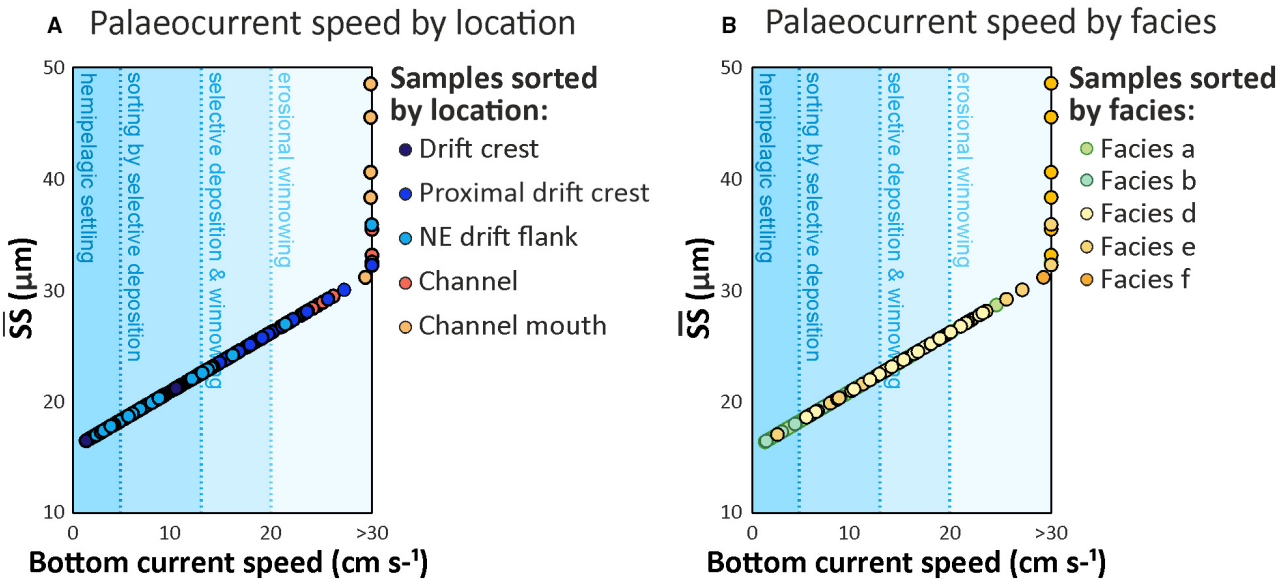

Fig. 13. Mean sortable silt ($\overline{SS}$) versus bottom current speed (cm s^{-1}) distinguished by location (A) and by facies (B). Bottom current speed boundaries for sorting and winnowing after McCave & Hall (2006), McCave (2008) and McCave *et al.* (2017). Note that the SS current meter of McCave *et al.* (2017) is not calibrated for bottom-current velocities exceeding *ca* 25 cm s^{-1}. Depths of discrete grain size samples are marked in Fig. S2.

than the modern maximum (on average 16.5 cm s^{-1}, with a full range of 3 to >30 cm s^{-1} in Fig. 13). Above flow speeds of *ca* 15 cm s^{-1}, winnowing of fine-grained particles can occur, and above *ca* 20 cm s^{-1} erosion can set in (e.g. McCave & Hall, 2006; McCave, 2008). Therefore, the highest $\overline{SS}$ values reveal that the bottom currents must have been very high and capable of winnowing fine-grained particles.

Other studies have identified similar facies as plumites on the Svalbard–Barents Sea in the Northern Hemisphere (Lucchi *et al.*, 2013). The alternating silt/sand and clay with a progressive upward decrease of grain size were interpreted as a progressive retreat of the ice front across the adjacent shelf, due to ice sheet melting and decay. However, in our case, parallel-laminations and condensation across Facies-e suggest that these deposits were not plumites (Figs 6A and 14), as these traits are more often associated with bottom-current facies and current reworking (Hüneke *et al.*, 2020). The presence of fine-grained sediments and rare bioturbation (Fig. 3F) indicates that this facies probably derived from low density turbidites, which were redistributed by weak to moderate bottom currents and formed distinct laminations (Fig. 3F) and grain-size variations (Fig. 6A). These processes formed silty to sandy contourite layers through alternations of suspension and reworking/winnowing processes (Shanmugam *et al.*, 1993; Stow *et al.*, 2009; Hüneke *et al.*, 2020; de Castro *et al.*, 2021).

Reworked turbidites (Facies-f)

The fine to very coarse sandy beds with grain-size variations and erosional bases (Figs 3H and 6F) reflect mixed deposits, probably turbiditic in origin. The erosional basal boundaries (Fig. 3I and K) were probably formed by high energy turbidity currents or under the influence of a strong bottom current. Their proximity to the main submarine channels (Fig. 14) and the coarser grain sizes supports the former (Fig. 5), with a turbidity current eroding the seafloor through tractive processes and depositing coarse sediments (Stanley, 1987, 1988, 1993; Shanmugam *et al.*, 1993). However, the formation of wavy and parallel-laminations towards the centre of these beds (Figs 3I and 6D) points to superimposed, active winnowing or reworking by bottom currents. Furthermore, most intervals show coarsening-upward or fining-upward sequences (Fig. 14), typical of contourite deposits (Gonthier *et al.*, 1984; Martín-Chivelet *et al.*, 2008; de Castro *et al.*, 2020, 2021; Hüneke *et al.*, 2020). The relatively clean, moderately sorted, leptokurtic, coarse grain sizes (Fig. 6C and D) and mode of

© 2022 The Authors. *Sedimentology* published by John Wiley & Sons Ltd on behalf of International Association of Sedimentologists, *Sedimentology*, **69**, 1953–1991

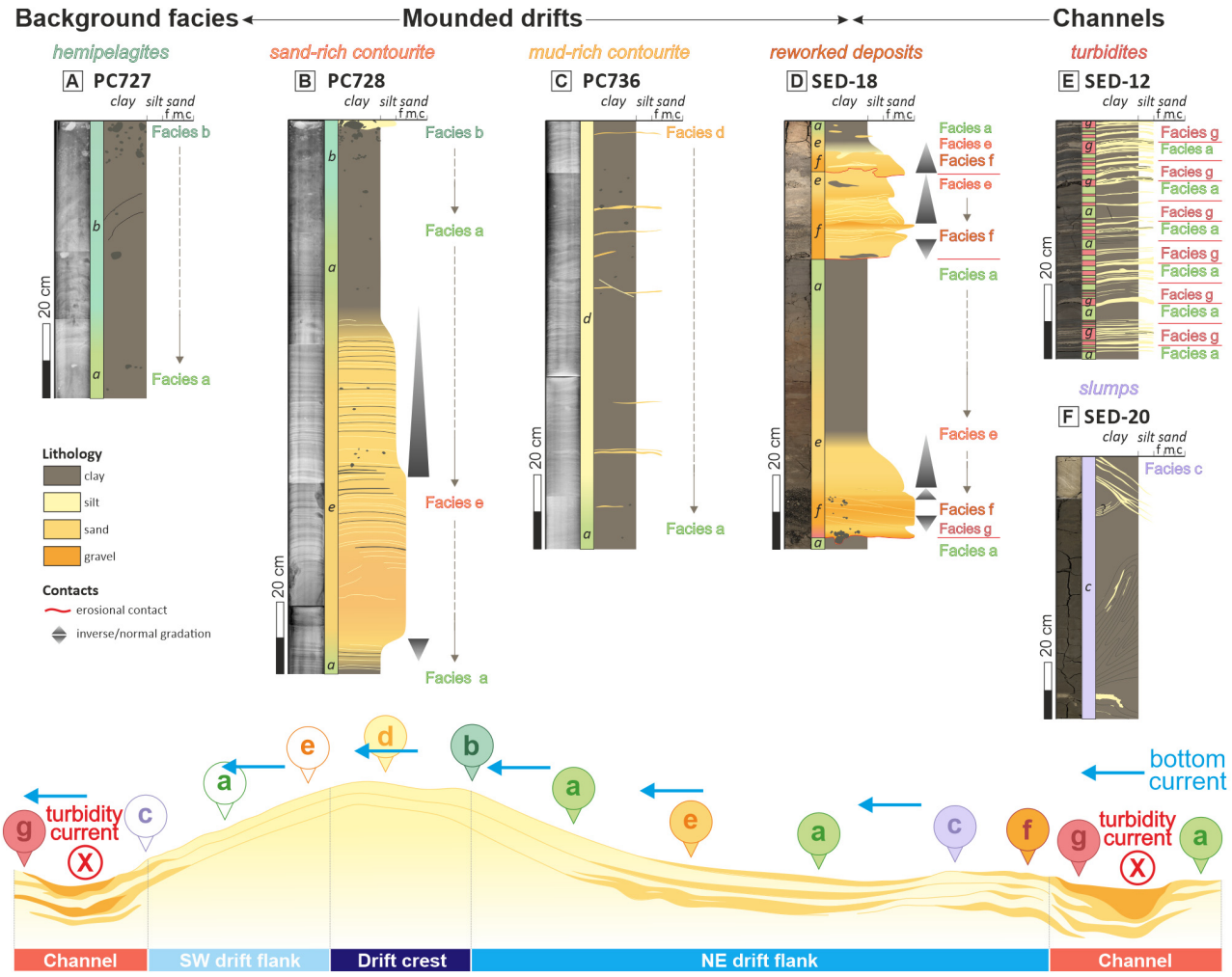

Fig. 14. Lateral and vertical variation of the main sedimentary facies across the mounded drifts and channels of the Pacific margin of the Antarctic Peninsula (PMAP) mixed systems. Coloured circles indicate facies based on the present study and open circles are based on previous seismic and sedimentological studies (Rebesco *et al.*, 1996, 1998, 2002; Lucchi *et al.*, 2002; Lucchi & Rebesco, 2007). Depth ranges of core intervals are given in Fig. 2.

ca 177.1 μm (Fig. 4) imply that saltation and traction contributed to the redistribution of the coarse-grained particles, while winnowing removed the fine-grained fraction (Brackenridge *et al.*, 2018; Hüneke *et al.*, 2020). The absence of sand infilled traces in the sandy intervals of Facies-f (Fig. 3I and K) implies high sedimentation rates and unfavourable environmental conditions for benthos due to active re-deposition by strong currents. Furthermore, rapid deposition of Facies-f is also supported by the absence of sand infilled traces into the underlying deposits (Fig. 3I).

The coarse-grained intervals with wavy laminations, high ln (Zr/Rb) and grain-size variations are characterized by high $\overline{SS}$ and SS% values (Fig. 12), suggesting a hydrodynamic regime with higher velocities than the modern bottom current speeds (Camerlenghi *et al.*, 1997; Giorgetti *et al.*, 2003), mostly >19.5 cm s^{-1} and up to >>30 cm s^{-1} (Fig. 13; McCave, 2008; Stow *et al.*, 2009; McCave *et al.*, 2017). Previous studies have interpreted similar facies as reworked turbidites (de Castro *et al.*, 2020; Fonnesu *et al.*, 2020). The turbidity currents were initially sourced by high terrigenous supply from the continental shelf and slope, and the turbidites were reworked after their initial deposition on the continental rise by an along-slope bottom current. The current formed sand-rich deposits during intervals of higher current speed, when the fine-grained particles were winnowed

© 2022 The Authors. *Sedimentology* published by John Wiley & Sons Ltd on behalf of International Association of Sedimentologists, *Sedimentology*, **69**, 1953–1991

(Pudsey, 2000; Lucchi *et al.*, 2002; Lucchi & Rebesco, 2007).

Gravitational deposits (turbidites and mass-transport deposits; Facies-c and g)

The interbedded fine to coarse-grained deposits with erosional bases (Fig. 5) are frequently deformed or tilted (Fig. 3D), suggesting that they originated from turbidity currents and mass-transport processes (Fig. 14). The combination of erosive contacts with flame structures and rip-up clasts (Figs 3 and 4) indicates repetitive erosive episodes (Stanley, 1988; Shanmugam *et al.*, 1993; Martín-Chivelet *et al.*, 2008). The preservation of delicate flame structures has been associated with hydraulic jumps and supercritical flows (Postma *et al.*, 2009; Postma & Kleverlaan, 2018). These episodes denote small-scale interruptions in sedimentation, probably caused by active turbidity currents that swept along the channel and past the lateral flanks of the mounded drifts (Fig. 14). Absence of bioturbation could be related to rapid sedimentation during turbiditic episodes or harsh environmental conditions, which hampered benthos activity. The subsequent deposition of fine-grained sediments resulted from suspension fall-out from decelerating turbidity currents (Stanley, 1987, 1988, 1993; Ito, 2002). The intercalations of thin-bedded turbidites and muddy hemipelagic deposits (Fig. 3G) suggest intermittent but frequent sediment-laden down-slope currents with deposition of fine-grained suspended particles. The deformed beds of Facies-c (Fig. 3D) indicate transitions between non-cohesive and cohesive behaviours or superimposed mass-transport processes (Haughton *et al.*, 2009; Mulder & Hüneke, 2014; Shanmugam, 2016). Mass-transport deposits can evolve sequentially from slides into debris flows and subsequently into turbidity currents (Facies-g; Fig. 4), due to ambient water entrainment or when they encounter hydraulic jumps along the margin (Wright & Anderson, 1982; Larter & Cunningham, 1993; Shanmugam, 2016). This interaction focuses the flow downward, leading to seafloor erosion, sediment bypass and distal deposition of coarse to fine-grained deposits (Fig. 15; Mutti, 1992; Barker *et al.*, 1999; Fonnesu *et al.*, 2020). The overlying bottom current is considerably weaker than the turbidity current, as it preferentially strips the fine-grained particles from the turbidity currents and transports them towards the south-west (Fig. 15), forming fine-grained contourites or reworked deposits (Fig. 14).

Facies associations and depositional elements

The PMAP mixed systems host three main facies associations, linked to their distinct morphological elements (for example, mounded drifts and/or submarine channels) and the main depositional processes acting in the area (Fig. 15): (i) *hemipelagic facies association*; (ii) *gravitational facies association*; and (iii) *bottom current and reworked facies association*.

Hemipelagic facies association

The hemipelagic facies association (Facies-a and Facies-b) was deposited along the entire continental margin (Figs 15 and 16). Most of the other sedimentary facies either transition into or alternate with the hemipelagic Facies-a and b (Fig. 3). Along the main trunk channels, channel-systems, or at the distal terminations of the drifts, hemipelagic deposits are frequently interrupted by turbidites or MTDs (Fig. 3G), which embody the gravitational facies association (Fig. 15).

Gravitational facies association

This facies association includes Facies-c and g (Fig. 3). In the PMAP mixed systems, the coarse-grained sandy gravitational deposits appear along the channel systems and at the mouth of the main submarine channels (Fig. 9A). The finer-grained deposits are absent, probably because a large amount of the fine-grained particles was captured from the suspension cloud by the bottom current and redistributed south-westward towards the adjacent mounded drifts (e.g. Rebesco *et al.*, 1996; Figs 3J and 14). This is supported by grain-size data (Figs 5 and 6), which show that the sandy sediments within the trunk channels have very low clay and silt contents, although these fractions are common in the adjacent drifts.

Turbidity currents typically carry coarse-grained particles at the base and head of the flow while the fine-grained particles are carried in a turbulent suspension cloud (Bouma, 1962; Mutti, 1992, 2011). A single turbidity current can deposit a sequence comprising up to five distinct internal divisions, Ta to Te, according to the Bouma sequence model (Bouma, 1962). The five divisions of the Bouma model comprise, from base to top, a massive, normally graded gravelly to sandy unit with an erosional base (= Ta) overlain by a sandy unit with parallel laminae (= Tb) and a sandy to silty unit with current ripples (= Tc), followed by a silty unit with upper parallel laminae (= Td) and

© 2022 The Authors. *Sedimentology* published by John Wiley & Sons Ltd on behalf of International Association of Sedimentologists, *Sedimentology*, **69**, 1953–1991

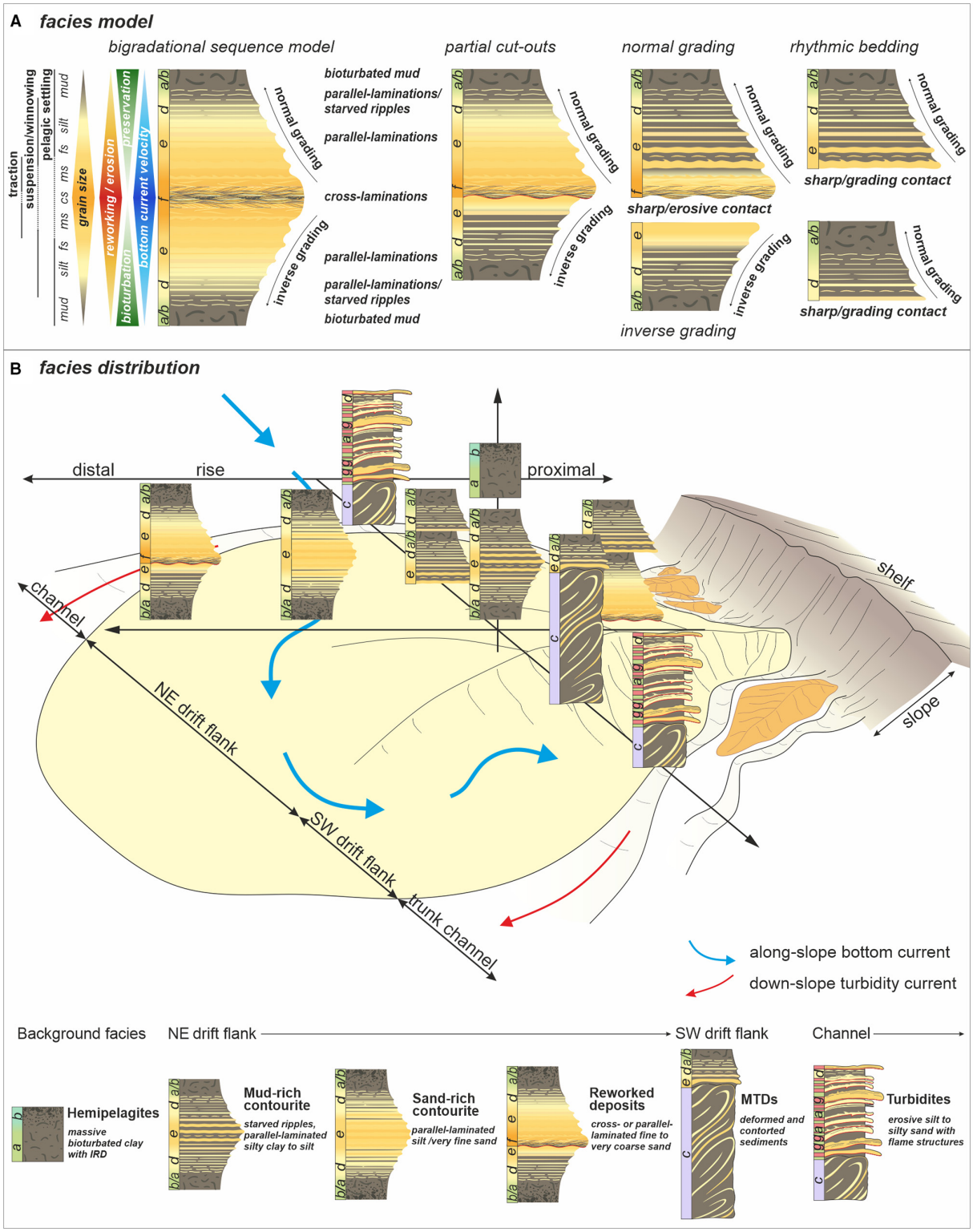

Fig. 15. Detailed sketch of the distinct sedimentary facies and their vertical and lateral distribution across the different morphological elements of the Pacific margin of the Antarctic Peninsula (PMAP) mixed systems (i.e. down-slope elongated, mounded drifts and trunk channels). The sedimentary facies across the north-east drift flanks, drift crests and channels are based on our interpretations, whereas the sedimentary facies on the south-west drift flanks are inferred from previous seismic and sedimentological studies (Rebesco *et al.*, 1996, 1998, 2002; Lucchi *et al.*, 2002; Lucchi & Rebesco, 2007).

© 2022 The Authors. *Sedimentology* published by John Wiley & Sons Ltd on behalf of International Association of Sedimentologists, *Sedimentology*, **69**, 1953–1991

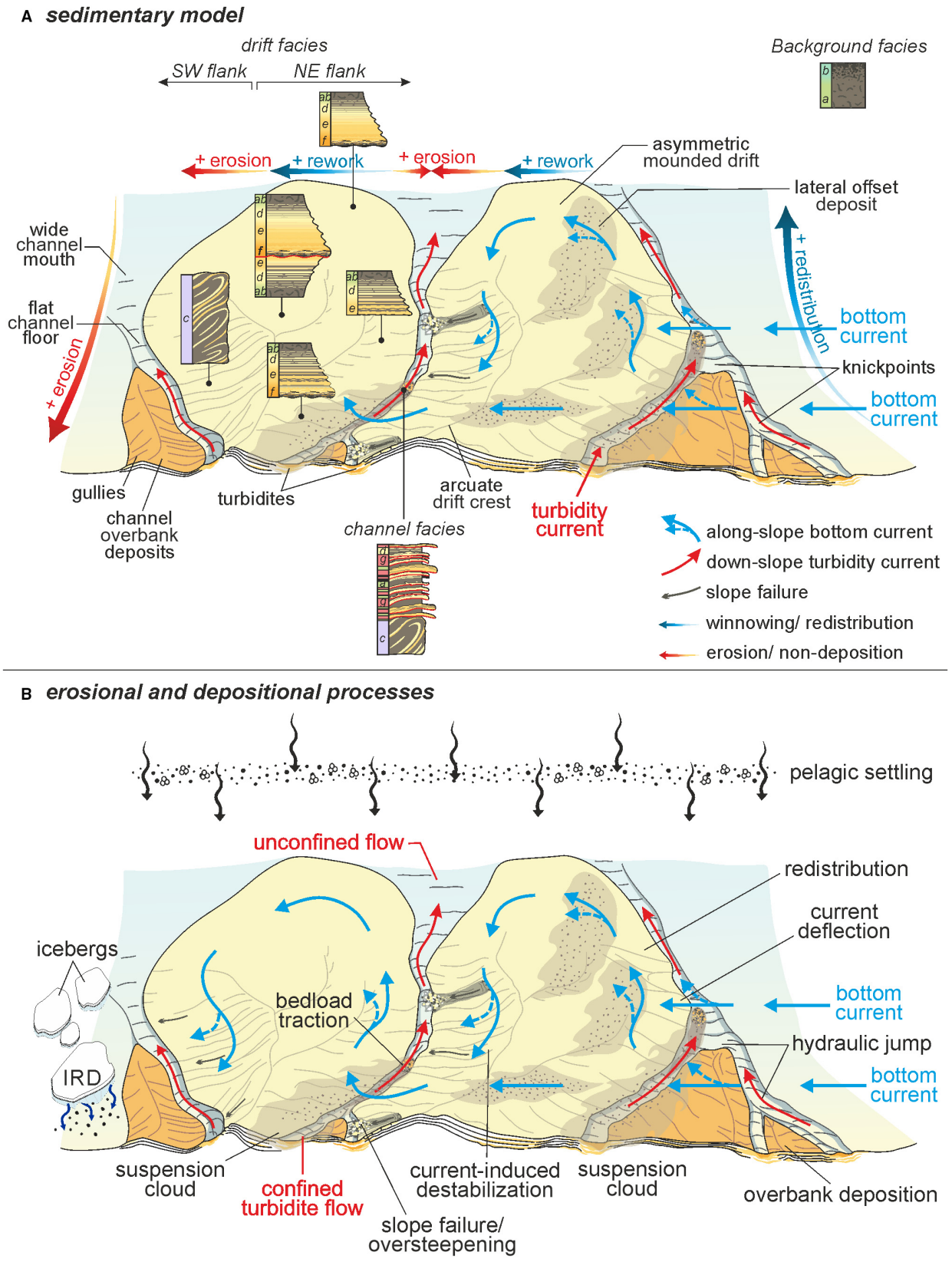

Fig. 16. Sedimentary model for the distribution of the sedimentary facies (A) and the processes (B) involved in their formation.

© 2022 The Authors. *Sedimentology* published by John Wiley & Sons Ltd on behalf of International Association of Sedimentologists, *Sedimentology*, **69**, 1953–1991

terminating in structureless or laminated mud (= Te) (Bouma, 1962; Mutti, 2011). The turbidites of Facies-g share certain traits with these divisions (Fig. 4), such as the erosional bases and parallel-laminations (Fig. 3G). However, the massive sands of Ta were not identified in the study area, and the same can be said for the gradual transition to Td and Te deposits (Fig. 3 J). Facies-g often has erosional top and base contacts with flame structures (Fig. 3G), which indicate erosion, hydraulic jumps or sediment bypass (Postma *et al.*, 2009; Postma & Kleverlaan, 2018). Moreover, this facies is usually winnowed by bottom currents (Fig. 16), which might explain the lack of fine-grained units Td and Te (Fig. 3J). It should be noted that similar interpretations have been mentioned for the Bouma sequence in the past, since each division could result from alternative sedimentation processes (Lowe, 1982; Shanmugam, 1997, 2016). For example, the pelagic sediments of Td and Te could result from bottom current reworking or hemipelagic settling during pauses or breaks of the down-slope turbiditic processes (Shanmugam, 1997, 2016; Mutti, 2011). This is corroborated by the occurrence of Facies-a in the submarine channels (Figs 3L and 14E), which originates mainly from hemipelagic settling.

The deformed beds of Facies-c (Fig. 3) also indicate the occurrence of other sediment gravity-driven processes (i.e. in addition to turbidity currents) across the margin, namely mass-transport processes (Fig. 15) such as slides, slumps and debris flows.

Bottom current and reworked facies association

This facies association includes Facies-d, e and f and represents, along with Facies-a and b, a bigradational sequence (Facies-d, e and f in Figs 3 and 6). This sequence comprises gradual transitions between facies, from a/b to d, e, f, and then back to e and d, before ending again in a/b facies (Fig. 14). In parallel, changes in the grain size and sedimentary structures also occur, from structureless clay to parallel-laminated silt and very fine sand (Fig. 14A), which transitions into wavy or cross-laminated fine to coarse sand (Fig. 14D) and then back into parallel-laminated silt and very fine sand, followed by structureless clay (Fig. 14B and C). These sequences are similar to those defined by Faugères *et al.* (1984) and Gonthier *et al.* (1984) for fine-grained contourites. The contourite model encompasses three main facies (homogeneous mud, mottled silt and mud, and sand and silt) arranged in a cyclic bigradational sequence that first coarsens upward and then fines upward (Gonthier *et al.*, 1984; Martín-Chivelet *et al.*, 2008; McCave, 2008; Rebesco *et al.*, 2014). These upward transitions have been interpreted as an increase and subsequent decrease of bottom current velocity (Stow *et al.*, 2002; Hüneke & Stow, 2008). The influence of bottom currents is similarly observed in our bigradational sequence (Fig. 15): the gradual transitions from clay to coarse sand, and the change from structureless to parallel-laminated and cross-laminated beds (Fig. 14), clearly indicates an increase in bottom current activity. Furthermore, these changes suggest that winnowing had an important role during the deposition of the initial (and final) fine-grained sediments (Facies-a, b, d and e), while saltation and traction played a more active role in the reworking of the coarser particles (Facies-f) and formed the cross-laminated sands at the centre of the sequence (Fig. 15). However, the bigradational contourite model lacks primary structures (Faugères *et al.*, 1984; Gonthier *et al.*, 1984). Intense bioturbation is probably responsible for their destruction, since oxygenated bottom currents provided environmental conditions suitable for benthic biota, which have bioturbated the sediments (Lucchi *et al.*, 2002; Lucchi & Rebesco, 2007; Rodríguez-Tovar & Hernández-Molina, 2018). In contrast, the bigradational sequence described here presents intense bioturbation and trace fossils only in muddy facies (Facies-a and b in Figs 3A and 14) and along the transitions between these facies and others (Facies-d and e in Fig. 3). This suggests a lower sedimentation rate and environmental conditions more favourable for benthic organisms during hemipelagic deposition. Conversely, the lack of bioturbation across the other sedimentary facies (Facies-d, e and f in Fig. 3) could be related to unfavourable conditions, such as lack of nutrients, or an increase in current energy and/or in the rate of sedimentation, which has prevented bioturbation. In fact, the lack of bioturbation for the other sedimentary facies is what probably allowed the preservation of their original sedimentary structures (Fig. 3). On glacially influenced margins, the presence, absence and/or degree of bioturbation is closely related to the environmental conditions and sedimentation rates (such as low and continuous sedimentation instead of high, rapid deposition) rather than bottom current activity (Lucchi & Rebesco, 2007; Hillenbrand *et al.*, 2021). Furthermore, the

© 2022 The Authors. *Sedimentology* published by John Wiley & Sons Ltd on behalf of International Association of Sedimentologists, *Sedimentology*, **69**, 1953–1991

presence of distinct sedimentary structures and changes in grain size (Fig. 6) across the contourites and reworked deposits (Fig. 14), show that the sedimentary record was affected by changes in sediment supply and bottom current activity, and was not affected or significantly reworked by benthic fauna.

The sediment source for most of these facies corresponds to flow-stripping of fine-grained suspended particles by the south-westward flowing bottom current from gravity-driven currents. The gravitational facies association is consistent with this process (Fig. 3G and H). The pirated clay to very fine sand fractions are redistributed across the north-east drift flanks (Fig. 14), where they form contourites and reworked deposits (Fig. 15). These deposits have lateral and vertical variations that derive from the mixture between sediment-laden gravity currents and bottom current reworking processes (Stanley, 1988; Shanmugam *et al.*, 1993; Viana *et al.*, 1998; Ito, 2002; Mutti *et al.*, 2014; de Castro *et al.*, 2020, 2021; Fonnesu *et al.*, 2020). In reality, these processes are highly dynamic and fluctuate over time, implying that more frequent gravity flows or stronger bottom current activity led to interruptions or partial cut-out sequences across the sedimentary record (Fig. 6D) as a result of current erosion, winnowing and/or reworking (Fig. 16). Partially reworked deposits with well-preserved sedimentary structures are typical of mixed systems (Shanmugam *et al.*, 1993; Viana *et al.*, 1998; Ito, 2002). Recent studies on mixed systems have proposed other facies models across distinct sedimentary settings (Mutti *et al.*, 2014; Gong *et al.*, 2016; de Castro *et al.*, 2020; Fonnesu *et al.*, 2020). The model presented here differs slightly from other models due to its location on the continental rise of a glacial margin (Fig. 1A) and due to the development of more complex and extensive morphological elements (Fig. 1B), which might be responsible for the preservation of these facies and their lateral or vertical variations (Fig. 15).

Sedimentary model for mixed/hybrid depositional systems

The distribution of three distinct facies associations across the PMAP mixed systems (Fig. 15) suggests that mixed/hybrid systems are built by recurrent interactions between hemipelagic, gravitational and bottom current processes (Fig. 16). Furthermore, frequent transitions, or alternations, between the different facies and facies associations (Fig. 14) reveal that mixed systems can comprise numerous deposits from different sources (such as hemipelagites, mud to sand-rich contourites, turbidites, reworked deposits or MTDs). As a result, the down-slope elongated, mounded drifts may comprise facies coarser than the typical contourite, while channels and channel-complex systems may hold deposits finer than the classic turbidite (Fig. 14). Their spatial and temporal variability allowed us to propose a sedimentary model for mixed/hybrid systems (Fig. 15).

For most mixed depositional systems, down-slope gravity-driven currents are the main sediment supplier (Gong *et al.*, 2013, 2016; Fonnesu *et al.*, 2020; Fuhrmann *et al.*, 2020). This is also the case for the PMAP mixed systems (Fig. 16). When grounded ice sheets advanced across the continental shelf during past glacial periods, they carried glaciogenic debris before depositing it at the mouths of palaeo-ice streams at or near the shelf break (Larter & Cunningham, 1993; Pudsey & Camerlenghi, 1998; Barker *et al.*, 1999, 2002; Pudsey, 2000; Amblas *et al.*, 2006; Hernández-Molina *et al.*, 2017). This material was then transported down-slope by gravitational mass-transport processes (Diviacco *et al.*, 2006; Rebesco & Camerlenghi, 2008). Furthermore, turbidity currents are frequently initiated at the base of the steep continental slope (Larter *et al.*, 1997; Dowdeswell *et al.*, 2004), and therefore turbidites and/or MTDs (Facies-c and g in Fig. 4) are deposited along the channel-complex systems, trunk channels and occasionally over the proximal flanks of the mounded drifts (Fig. 14). Gravitational processes may also have been triggered across the mounded drifts, especially along the steep flanks (Fig. 16), due to their high relief, moderate to high sedimentation rates (Table 2), and erosion from nearby channels. Previous studies support this interpretation, as MTDs, turbidites and slide scars were identified across the mounded drifts (Rebesco *et al.*, 1998, 2002; Lucchi *et al.*, 2002; Amblas *et al.*, 2006; Lucchi & Rebesco, 2007; Larter *et al.*, 2016).

The down-slope gravity-driven currents eventually meet the south-westward flowing bottom current, which entrains and redistributes the fine-grained particles carried in suspension by the gravity flows (Fig. 16; Rebesco *et al.*, 1996; Pudsey, 2000). Modern current meter measurements indicate that a generally south-westward directed bottom current contours the mounded

© 2022 The Authors. *Sedimentology* published by John Wiley & Sons Ltd on behalf of International Association of Sedimentologists, *Sedimentology*, **69**, 1953–1991

drifts from the seafloor up to 60 m above (Fig. 1A; Camerlenghi *et al.*, 1997; Giorgetti *et al.*, 2003; Hillenbrand *et al.*, 2008a). This bottom current has a low average current speed at present, around *ca* 6 cm s^{-1} (and up to 20 cm s^{-1}), according to Camerlenghi *et al.* (1997) and Giorgetti *et al.* (2003). However, it would have reached speeds >30 cm s^{-1} in the past (Fig. 13), as shown by the wide range of $\overline{SS}$ and SS% values in our data (Fig. 12). Hydrodynamic fluctuations of the bottom current probably generated gradual transitions between mud-rich and sand-rich contourites across the mounded drifts (Fig. 15), with cross to ripple-laminated primary structures (Facies-d and e in Fig. 3). Furthermore, the coarser deposits (Facies-f in Fig. 3I and K) would require higher bottom-current velocities [>>30 cm s^{-1} in Fig. 13, according to McCave (2008), Stow *et al.* (2009) and McCave *et al.* (2017)] to winnow the medium to coarse-grained turbidites accumulated along the trunk channels and over their margins (Fig. 14). A coarse lag may remain at the base from the original turbidite deposit (such as the granules at the base of Facies-f in Fig. 3I and K) while the bottom current strips the fine-grained particles and creates mud to sand-rich deposits with parallel and cross-laminations. (Facies-f in Figs 3I and 14D).

Periodic switches or breaks in the sediment supply (for example, of the gravitational processes) would allow interactions between hemipelagic settling, meltwater plumes and weak bottom current activity to form extensive hemipelagic deposits and/or mud-rich contourites (Facies-a, b and d in Fig. 3) across the mixed systems (Pudsey & Camerlenghi, 1998; Hillenbrand & Ehrmann, 2001; Lucchi *et al.*, 2002; Amblas *et al.*, 2006; Cowan *et al.*, 2008; Vautravers *et al.*, 2013). These deposits cover the previously accumulated sediments (Fig. 14) and allow for the preservation of their primary structures.

At the time of deposition, the suspended particles are affected by the most dominant process; however, the persistence of bottom-currents ultimately leads to redistribution and reworking of most deposits, and especially of fine-grained sediments carried in suspension (Fig. 16). The distinct sedimentary facies identified in this study (Fig. 14) reflect the fluctuations of the different sedimentary processes (Fig. 16), in terms of their velocity, frequency, direction, range of effect and persistence over time.

Controlling factors

Alternations throughout the sedimentary record (Figs 11 and S2) indicate cyclic variations involving gravitational deposits (turbidites of Facies-g and MTDs of Facies-c in Fig. 3), reworked deposits (Facies-f in Fig. 3), contourites (Facies-d and e in Fig. 3) and hemipelagites (Facies-a and b in Fig. 3). The presence of biogenic material and IRD across certain intervals of Facies-a and b (Fig. 3A and section '1') indicates hemipelagic deposition with little turbiditic input during interglacials (Ó Cofaigh *et al.*, 2001; Lucchi *et al.*, 2002; Lucchi & Rebesco, 2007; Cowan *et al.*, 2008; Vautravers *et al.*, 2013), while intervals with faint laminations and without bioturbation or biogenic material indicate glacial periods (Figs 11 and S2). The same can be said for Facies-d and e, which have abundant primary structures and rare bioturbation (Fig. 3) and therefore support bottom current redeposition and reworking of sediments during glacial periods (Lucchi *et al.*, 2002; Lucchi & Rebesco, 2007). Facies-f is characterized by normal or inverse grading of parallel to cross-laminated coarse sands without bioturbation or biogenic material (Fig. 6C), and its deposition probably resulted from an active and strong bottom current, which was able to remobilize coarse-grained particles. The sediment intervals with the three major Facies-f horizons identified in this study (Figs 3, 6 and 9A) have been assigned to glacial Marine Isotope Stages (MIS) 2 to 4 and MIS-6 (Fig. 11; cf. Lucchi *et al.*, 2002). Therefore, recurring sedimentary facies (such as Facies-a, d, e and f in Fig. 14) record repetitive episodes of pelagic settling processes, along-slope current activity and down-slope gravitational processes (Fig. 16), driven by glacial–interglacial changes (Fig. 11). Previous seismic studies by Rebesco *et al.* (2002), Uenzelmann-Neben (2006) and Hernández-Molina *et al.* (2017) agree with this interpretation, deeming glacial to interglacial changes fundamental for the shift between dormant and active down-slope and along-slope processes. In the sedimentological studies by Pudsey & Camerlenghi (1998), Pudsey (2000, 2002), Hillenbrand & Ehrmann (2001), Ó Cofaigh *et al.* (2001), Lucchi *et al.* (2002), Lucchi & Rebesco (2007) and Hillenbrand *et al.* (2021), cyclic variations of grain size, sedimentary structures, biogenic content, clay mineral provenance and IRD supply have been associated with changes in sea-ice cover and grounded ice-sheet advance/retreat

© 2022 The Authors. *Sedimentology* published by John Wiley & Sons Ltd on behalf of International Association of Sedimentologists, *Sedimentology*, **69**, 1953–1991

across the adjacent continental shelf, implying that glaciations and deglaciations are responsible for variations in the supply of both terrigenous and biogenic particles. Other high-latitude mixed systems have presented similar results, where changes in sedimentary facies and morphological features are associated with fluctuations in turbidity currents or along-slope bottom current activity (Clausen, 1998; Escutia *et al.*, 2000; Michels *et al.*, 2001; Rasmussen *et al.*, 2003; Forwick *et al.*, 2015; García *et al.*, 2016; Salabarnada *et al.*, 2018). Climatic and sea-level oscillations have also been tied to significant changes in turbidity current flows (Hubbard *et al.*, 2014) and to the hydrodynamic fluctuations of the bottom current (de Castro *et al.*, 2021). Across mid-latitude mixed systems, interactions between along-slope and down-slope processes are frequent (Ito, 2002; Donda *et al.*, 2008; Brackenridge *et al.*, 2013; Gong *et al.*, 2013, 2016; Palamenghi *et al.*, 2015; Miramontes *et al.*, 2019; Fuhrmann *et al.*, 2020), but few studies have investigated the influence of glacial–interglacial changes in their stratigraphic stacking patterns and sedimentary records (Marchès *et al.*, 2010; Calvès *et al.*, 2013; Mena *et al.*, 2018; Tallobre *et al.*, 2019). These studies have reached similar conclusions, supporting an interplay of deep-water processes, driven by climatic and sea-level oscillations (Marchès *et al.*, 2010; Calvès *et al.*, 2013; Mena *et al.*, 2018; Tallobre *et al.*, 2019).

CONCLUSIONS

Research into mixed or hybrid sedimentary facies has faced difficulties in the past due to the challenge of identifying clear, diagnostic criteria and differentiating the deep-water processes behind their formation.

The dominant facies and facies associations identified along the Pacific margin of the Antarctic Peninsula (PMAP) mixed systems reflect fluctuations between three key deep-water processes: along-slope bottom currents, down-slope gravity-driven currents and hemipelagic settling. A clear link between the distinct sedimentary facies and the different morphological features (i.e. mounded drifts, channels and channel systems) results from the fluctuating interactions between along-slope and down-slope processes, across time and space. Mounded drifts comprise hemipelagites, contourites and bottom-current reworked deposits, while channels and channel-systems hold thin-bedded turbidites and other gravitational deposits, such as slumps.

Lateral and temporal variations of along-slope and down-slope processes were responsible for a cyclic depositional pattern, which has been linked to glacial–interglacial environmental changes during the Late Quaternary. The frequency of gravitational processes and the higher velocity of bottom currents have been tied to glacial periods (MIS 2 to 4 and 6), as the accumulation of glaciogenic debris at the mouths of palaeo-ice streams provided greater down-slope sediment supply when the grounded ice streams had advanced towards the continental shelf break.

The sedimentary record on polar margins is key to better understand the effects of bottom currents in the deposition of fine to coarse-grained sediments, as the scarcity of bioturbation allows us to observe the original sedimentary structures, which are poorly preserved in similar deposits across non-polar continental margins. Diagnostic criteria such as grain-size variations, bigradational sequences, parallel to cross-laminations, contact surfaces, sedimentary condensation, ichnological features and degree of bioturbation are key evidence for the detection of bottom current processes (i.e. entrainment, winnowing, reworking and fluctuating hydrodynamic conditions), as well as its differentiation from other deep-water processes in the sedimentary record. Further sedimentological, ichnological and geochemical analyses should be conducted in other mixed/hybrid depositional systems to provide a better understanding of the spatial and temporal variability of their deposits and the interplay of deep-water processes.

ACKNOWLEDGEMENTS

This project was funded through the Joint Industry Project (JIP) supported by BP (United Kingdom), ENI (Italy), TOTAL (France), ExxonMobil (United States), Wintershall Dea (Germany), and TGS (United Kingdom) within the framework of 'The Drifters' Research Group at Royal Holloway, University of London (RHUL), and it is related to the TASDRACC Project CTM2017-89711-C2-01-P & CTM2017-89711-C2-02-P. Research by R. Larter and C.-D. Hillenbrand was funded through NERC UK-IODP Site Survey Investigation grant NE/JOO6548/1 and the 'Polar Science for Planet Earth' programme of the British Antarctic Survey. Research by F. Rodríguez-Tovar was funded by

© 2022 The Authors. *Sedimentology* published by John Wiley & Sons Ltd on behalf of International Association of Sedimentologists, *Sedimentology*, **69**, 1953–1991

Project PID2019-104625RB-100 (Secretaría de Estado de I + D+I, Spain), B-RNM-072-UGR18 (FEDER Andalucía), and P18-RT-4074 (Junta de Andalucía). Research by R.G. Lucchi and M. Rebesco was funded by the PNRA Project 16_00205 (ODYSSEA). This research used samples and data collected through the PNRA SEDANO-II Project and the NERC UK-IODP Site Survey Investigation expedition JR298. We would like to thank Stefano Miserochi for his assistance with the XRF analyses at the CNR-ISMAR in Bologna (Italy), Ester Colliza for her assistance with the handling of the SEDANO-II cores handling at the Sorting Centre of the National Antarctic Museum in Trieste (Italy), Dr Emmanuelle Ducassou and Dr Marie-Claire Perello (Univ. Bordeaux, France) for conducting the grain size measurements, and Prof. Nick McCave (Univ. Cambridge, UK) for his help in calculating and understanding the sortable silt method. We also thank the captain, officers, crew, support staff and scientists who participated in the research cruises that provided data for this study. Finally, we thank the Editor and two reviewers for their positive and useful suggestions which helped us improve this manuscript.

CONFLICT OF INTEREST

We declare that we have no commercial or associative aim that might represent a conflict of interest in connection with the work submitted.

DATA AVAILABILITY STATEMENT

The data that support the findings of this study are available from the corresponding author upon reasonable request. The XRF data, cluster analyses and PCA are openly available in Mendeley Data at http://doi.org/10.17632/524cr43x9j.1.

REFERENCES

Aitchison, J. (1986) Calibration of XRF core scanners for quantitative geochemical logging of sediment cores: theory and application. *Earth Planet. Sci. Lett.*, **274**, 423–438. https://doi.org/10.1016/j.epsl.2008.07.054

Amblas, D., **Urgeles, R.**, **Canals, M.**, **Calafat, A.M.**, **Rebesco, M.**, **Camerlenghi, A.**, **Estrada, F.**, **De-Batist, M.** and **Hughes-Clarke, J.E.** (2006) Relationship between continental rise development and palaeo-ice sheet dynamics, northern Antarctic Peninsula Pacific margin. *Quatern. Sci. Rev.*, **25**, 933–944. https://doi.org/10.1016/j.quascirev.2005.07.012

Baas, J.H., **Best, J.L.** and **Peakall, J.** (2016) Predicting bedforms and primary current stratification in cohesive mixtures of mud and sand. *J. Geol. Soc.*, **173**, 12–45. https://doi.org/10.1144/jgs2015-024

Barker, P.F., **Camerlenghi, A.** and **Leg 178 Scientific Party**. (1999) *Initial Reports, Ocean Drilling Program, 178*. Ocean Drilling Program, College Station, TX, 90 pp.

Barker, P.F., **Camerlenghi, A.**, **Acton, G.D.** and **Ramsay, A.T.S.** (2002) *Proceedings of the Ocean Drilling Program, Scientific Results, 178*, pp. 77845–79547. Ocean Drilling Program, College Station, TX.

Blott, S.J. and **Pye, K.** (2001) Gradistat: a grain size distribution and statistic package for the analysis of unconsolidated sediments. *Earth Surf. Proc. Land*, **26**, 1237–1248. https://doi.org/10.1002/esp.261

Bouma, A.H. (1962) Sedimentology of some flysch deposits. In: *A Graphic Approach to Facies Interpretation* (Ed. Bouma, A.H.). Elsevier, Amsterdam/New York, 168 pp.

Brackenridge, R.E., **Hernández-Molina, F.J.**, **Stow, D.A.V.** and **Llave, E.** (2013) A Pliocene mixed contourite-turbidite system offshore the Algarve Margin, Gulf of Cadiz: seismic response, margin evolution and reservoir implications. *Mar. Petrol. Geol.*, **46**, 36–50. https://doi.org/10.1016/j.marpetgeo.2013.05.015

Brackenridge, R.E., **Stow, D.A.**, **Hernández-Molina, F.J.**, **Jones, C.**, **Mena, A.**, **Alejo, I.**, **Ducassou, E.**, **Llave, E.**, **Ercilla, G.**, **Nombela, M.A.**, **Pérez-Arlucea, M.** and **Frances, G.** (2018) Textural characteristics and facies of sand-rich contourite depositional systems. *Sedimentology*, **65**, 2223–2252. https://doi.org/10.1111/sed.12463

Calvès, G., **Toucanne, S.**, **Jouet, G.**, **Charrier, S.**, **Thereau, E.**, **Etoubleau, J.**, **Marsset, T.**, **Droz, L.**, **Bez, M.**, **Abreu, V.**, **Jorry, S.**, **Mulder, T.** and **Lericolais, G.** (2013) Inferring denudation variations from the sediment record: an example of the last glacial cycle record of the Golo Basin and watershed, East Corsica, western Mediterranean Sea. *Basin Res.*, **25**, 197–218. https://doi.org/10.1111/j.1365-2117.2012.00556.x

Camerlenghi, A., **Crise, A.**, **Pudsey, C.J.**, **Accerboni, E.**, **Laterza, R.** and **Rebesco, M.** (1997) Ten-month observation of the bottom current regime across a sediment drift of the Pacific margin of the Antarctic Peninsula. *Antarct. Sci.*, **9**, 426–433. https://doi.org/10.1017/S0954102097000552

de Castro, S., **Hernández-Molina, F.J.**, **Rodríguez-Tovar, F.J.**, **Llave, E.**, **Ng, Z.L.**, **Nishida, N.** and **Mena, A.** (2020) Contourites and bottom current reworked sands: bed facies model and implications. *Mar. Geol.*, **428**, 106267. https://doi.org/10.1016/j.margeo.2020.106267

de Castro, S., **Hernández-Molina, F.J.**, **de Weger, W.**, **Jiménez-Espejo, F.J.**, **Rodríguez-Tovar, F.J.**, **Mena, A.**, **Llave, E.** and **Sierro, F.J.** (2021) Contourite characterization and its discrimination from other deep-water deposits in the Gulf of Cadiz contourite depositional system. *Sedimentology*, **68**, 987–1027. https://doi.org/10.1111/sed.12813

Cauxeiro, C., **Lopez, M.**, **Hernández-Molina, F.J.**, **Miguel, A.**, **Cauxeiro, G.** and **Caetano, V.** (2020) Contourite Vs. Turbidite Outcrop and Seismic Architectures. *Angolan Min. Oil Gas J.*, **1**, 20–26. https://doi.org/10.47444/amogj.v1i1.9

Channell, J.E.T., **Xuan, C.**, **Hodell, D.A.**, **Crowhurst, S.J.** and **Larter, R.D.** (2019) Relative paleointensity (RPI) and age control in Quaternary sediment drifts off the Antarctic

Peninsula. *Quatern. Sci. Rev.*, **211**, 17–33. https://doi.org/10.1016/j.quascirev.2019.03.006

Clausen, L. (1998) The Southeast Greenland glaciated margin: 3D stratal architecture of shelf and deep sea. In: *Geological Processes on Continental Margins: Sedimentation, Mass-Wasting and Stability* (Eds Stoker, M., Evans, D. and Cramp, A.), *Geol. Soc. London Spec. Publ.*, **129**, 173–203. https://doi.org/10.1144/GSL.SP.1998.129.01.12

Cowan, E.A., **Hillenbrand, C.-D.**, **Hassler, L.E.** and **Ake, M.T.** (2008) Coarse-grained terrigenous sediment deposition on continental rise drifts: a record of Plio-Pleistocene glaciation on the Antarctic Peninsula. *Palaeogeogr. Palaeoclimatol. Palaeoecol.*, **265**, 275–291. https://doi.org/10.1016/j.palaeo.2008.03.010

Creaser, A., **Hernández-Molina, F.J.**, **Badalini, G.**, **Thompson, P.**, **Walker, R.**, **Soto, M.** and **Conti, B.** (2017) A late Cretaceous mixed (turbidite-contourite) system along the Uruguayan Margin: sedimentary and palaeoceanographic implications. *Mar. Geol.*, **390**, 234–253. https://doi.org/10.1016/j.margeo.2017.07.004

Diviacco, P., **Rebesco, M.** and **Camerlenghi, A.** (2006) Late Pliocene mega debris flow deposit and related fluid escapes identified on the Antarctic Peninsula continental margin by seismic reflection data analysis. *Mar. Geophys. Res.*, **27**, 109–128. https://doi.org/10.1007/s11001-005-3136-8

Donda, F., **O'Brien, P.E.**, **De Santis, L.**, **Rebesco, M.** and **Brancolini, G.** (2008) Mass wasting processes in the Western Wilkes Land margin: possible implications for East Antarctic glacial history. *Palaeogeogr. Palaeoclimatol. Palaeoecol.*, **260**, 77–91. https://doi.org/10.1016/j.palaeo.2007.08.008

Donohue, K.A., **Tracey, K.L.**, **Watts, D.R.**, **Chidichimo, M.P.** and **Chereskin, T.K.** (2016) Mean Antarctic circumpolar current transport measured in drake passage. *Geophys. Res. Lett.*, **43**, 760–767. https://doi.org/10.1002/2016GL070319

Dorador, J., **Rodríguez-Tovar, F.J.** and **IODP Expedition 339 Scientists**. (2014a) Digital image treatment applied to ichnological analysis of marine core sediments. *Facies*, **60**, 39–44. https://doi.org/10.1007/s10347-013-0383-z

Dorador, J., **Rodríguez-Tovar, F.J.** and **IODP Expedition 339 Scientists** (2014b) Quantitative estimation of bioturbation based on digital image analysis. *Mar. Geol.*, **349**, 55–60. https://doi.org/10.1016/j.margeo.2014.01.003

Dorador, J. and **Rodríguez-Tovar, F.J.** (2018) High-resolution image treatment in ichnological core analysis: initial steps, advances and prospects. *Earth-Sci. Rev.*, **177**, 226–237. https://doi.org/10.1016/j.earscirev.2017.11.020

Dowdeswell, J.A., **Ó Cofaigh, C.** and **Pudsey, C.** (2004) Continental slope morphology and sedimentary processes at the mouth of an Antarctic palaeo-ice stream. *Mar. Geol.*, **204**, 203–214. https://doi.org/10.1016/S0025-3227(03)00338-4

Escutia, C., **Eittreim, S.L.**, **Cooper, A.K.** and **Nelson, C.H.** (2000) Morphology and acoustic character of the Antarctic Wilkes Land turbidite systems: ice-sheet-sourced versus river-sourced fans. *J. Sed. Res.*, **70**, 84–93. https://doi.org/10.1306/2DC40900-0E47-11D2-8643000102C1865D

Faugères, J.C., **Gonthier, E.** and **Stow, D.A.V.** (1984) Contourite drift molded by deep Mediterranean outflow. *Geology*, **12**, 296–300. https://doi.org/10.1130/0091-7613(1984)12<296:CDMBDM>2.0.CO;2

Faugères, J.-C., **Stow, D.A.V.**, **Imbert, P.** and **Viana, A.R.** (1999) Seismic features diagnostic of contourite drifts. *Mar. Geol.*, **162**, 1–38. https://doi.org/10.1016/S0025-3227(99)00068-7

Faugères, J.-C. and **Stow, D.A.V.** (2008) Contourite drifts: nature, evolution and controls. In: *Contourites* (Eds Rebesco, M. and Camerlenghi, A.), *Dev. Sedimentol.*, **60**, 257–288. doi: https://doi.org/10.1016/S0070-4571(08)10014-0

Folk, R. and **Ward, W.** (1957) Brazos River Bar: a study in the significance of grain size parameters. *J. Sed. Petrol.*, **27**, 3–26. https://doi.org/10.1306/74D70646-2B21-11D7-8648000102C1865D

Fonnesu, M., **Palermo, D.**, **Galbiati, M.**, **Marchesini, M.**, **Bonamini, E.** and **Bendias, D.** (2020) A new world-class deep-water play-type, deposited by the syndepositional interaction of turbidity flows and bottom currents: the giant Eocene Coral Field in northern Mozambique. *Mar. Petrol. Geol.*, **111**, 179–201. https://doi.org/10.1016/j.marpetgeo.2019.07.047

Forwick, M., **Laberg, J.S.**, **Hass, H.C.** and **Osti, G.** (2015) The Kongsfjorden Channel System offshore NW Svalbard: downslope sedimentary processes in a contour-current-dominated setting. *Arktos*, **1**, 1–17. https://doi.org/10.1007/s41063-015-0018-4

Fuhrmann, A., **Kane, I.A.**, **Clare, M.A.**, **Ferguson, R.A.**, **Schomacker, E.**, **Bonamini, E.** and **Contreras, F.A.** (2020) Hybrid turbidite-drift channel complexes: an integrated multiscale model. *Geology*, **48**, 562–568. https://doi.org/10.1130/G47179.1

Gales, J.A., **Forwick, M.**, **Laberg, J.S.**, **Vorren, T.O.**, **Larter, R.D.**, **Graham, A.G.C.**, **Baeten, N.J.** and **Amundsen, H.B.** (2013) Arctic and Antarctic submarine gullies – a comparison of high latitude continental margins. *Geomorphology*, **201**, 449–461. https://doi.org/10.1016/j.geomorph.2013.07.018

García, M., **Dowdeswell, J.A.**, **Noormets, R.**, **Hogan, K.A.**, **Evans, J.**, **Ó Cofaigh, C.** and **Larter, R.** (2016) Geomorphic and shallow-acoustic investigation of an Antarctic Peninsula fjord system using high-resolution ROV and shipboard geophysical observations: Ice dynamics and behaviour since the Last Glacial Maximum. *Quatern. Sci. Rev.*, **153**, 122–138. https://doi.org/10.1016/j.quascirev.2016.10.014

General Bathymetric Chart of the Oceans. (2019) GEBCO 2019 Grid. Available online at: www.gebco.net. doi: https://doi.org/10.5285/836f016a-33be-6ddc-e053-6c86abc0788e

Giorgetti, G., **Crise, A.**, **Laterza, R.**, **Perini, L.**, **Rebesco, M.** and **Camerlenghi, A.** (2003) Water masses and bottom boundary layer dynamics above a sediment drift of the Antarctic Peninsula Pacific Margin. *Antarct. Sci.*, **15**, 537–546. https://doi.org/10.1017/S0954102003001652

Gong, C., **Wang, Y.**, **Zhu, W.**, **Li, W.** and **Xu, Q.** (2013) Upper Miocene to Quaternary unidirectionally migrating deep-water channels in the Pearl River Mouth Basin, northern South China Sea. *AAPG Bull.*, **97**, 285–308. https://doi.org/10.1306/07121211159

Gong, C., **Wang, Y.**, **Zheng, R.**, **Hernández-Molina, F.J.**, **Li, Y.**, **Stow, D.A.V.**, **Xu, Q.** and **Brackenridge, R.** (2016) Middle Miocene reworked turbidites in the Baiyun Sag of the Pearl River Mouth Basin, northern China Sea margin: processes, genesis, and implications. *J. Asian Earth Sci.*, **128**, 116–129. https://doi.org/10.1016/j.jseaes.2016.06.025

Gonthier, E.G., **Faugères, J.C.** and **Stow, D.A.V.** (1984) Contourite facies of the Faro drift, Gulf of Cadiz. *Geol. Soc. Lond. Spec. Publ.*, **15**, 275–292.

Hanquiez, V., **Mulder, T.**, **Toucanne, S.**, **Lecroart, P.**, **Bonnel, C.**, **Marchès, E.** and **Gonthier, E.** (2010) The sandy channel-lobe depositional systems in the Gulf of Cadiz:

© 2022 The Authors. *Sedimentology* published by John Wiley & Sons Ltd on behalf of International Association of Sedimentologists, *Sedimentology*, **69**, 1953–1991

gravity processes forced by contour current processes. *Sed. Geol.*, **229**, 110–123. https://doi.org/10.1016/j.sedgeo.2009.05.008

Haughton, P., **Davis, C.**, **McCaffrey, W.** and **Barker, S.** (2009) Hybrid sediment gravity flow deposits – classification, origin and significance. *Mar. Petrol. Geol.*, **26**, 1900–1918. https://doi.org/10.1016/j.marpetgeo.2009.02.012

Hebbeln, D., **Van Rooij, D.** and **Wienberg, C.** (2016) Good neighbours shaped by vigorous currents: cold-water coral mounds and contourites in the North Atlantic. *Mar. Geol.*, **378**, 171–185. https://doi.org/10.1016/j.margeo.2016.01.014

Hernández-Molina, F.J., **Larter, R.D.** and **Maldonado, A.** (2017) Neogene to quaternary stratigraphic evolution of the Antarctic Peninsula, Pacific Margin offshore of Adelaide Island: transitions from a non-glacial, through glacially-influenced to a fully glacial state. *Global Planet. Change*, **156**, 80–111. https://doi.org/10.1016/j.gloplacha.2017.07.002

Heroy, D.C. and **Anderson, J.B.** (2005) Ice-sheet extent of the Antarctic Peninsula region during the Last Glacial Maximum (LGM) – insights from glacial geomorphology. *Geol. Soc. Am. Bull.*, **117**, 1497–1512. https://doi.org/10.1130/B25694.1

Hillenbrand, C.-D., **Camerlenghi, A.**, **Cowan, E.A.**, **Hernández-Molina, F.J.**, **Lucchi, R.G.**, **Rebesco, M.** and **Uenzelmann-Neben, G.** (2008a) The present and past bottom-current flow regime around the sediment drifts on the continental rise west of the Antarctic Peninsula. *Mar. Geol.*, **255**, 55–63. https://doi.org/10.1016/j.margeo.2008.07.004

Hillenbrand, C.-D., **Crowhurst, S.J.**, **Williams, M.**, **Hodell, D.A.**, **McCave, I.N.**, **Ehrmann, W.**, **Xuan, C.**, **Piotrowski, A.M.**, **Hernández-Molina, F.J.**, **Graham, A.G.C.**, **Grobe, H.**, **Williams, T.J.**, **Horrocks, J.R.**, **Allen, C.S.** and **Larter, R.D.** (2021) New multi-proxy data from West Antarctic drift sediments: implications for dating and interpreting Late Quaternary palaeoenvironmental records from the Antarctic margin. *Glob. Planet. Change*, **257**, 106482. https://doi.org/10.1016/j.quascirev.2021.106842

Hillenbrand, C.-D. and **Ehrmann, W.** (2001) Distribution of clay minerals in drift sediments on the continental rise west of the Antarctic Peninsula, ODP Leg 178, Sites 1095, 1096, and 1101. In: *Proc. ODP Sci. Results* (Eds Barker, P.F., Camerlenghi, A., Acton, G.D. and Ramsay, A.T.S.), **178**, 1–33. doi:https://doi.org/10.2973/odp.proc.sr.178.215.2001

Hillenbrand, C.-D., **Moreton, S.G.**, **Caburlotto, A.**, **Pudsey, C.J.**, **Lucchi, R.G.**, **Smellie, J.L.**, **Benetti, S.**, **Grobe, H.**, **Hunt, J.B.** and **Larter, R.D.** (2008b) Volcanic time-markers for marine isotopic stages 6 and 5 in Southern Ocean sediments and Antarctic ice cores: implications for tephra correlations between palaeoclimatic records. *J. Quat. Sci. Rev.*, **27**, 518–540. https://doi.org/10.1016/j.quascirev.2007.11.009

Hodell, D.A., **Nicholl, J.A.**, **Bontognali, R.R.R.**, **Danino, S.**, **Dorador, J.**, **Dowdeswell, J.A.**, **Einsle, J.**, **Kuhlmann, H.**, **Martrat, B.**, **Mleneck-Vautravers, M.J.**, **Rodríguez-Tovar, F.J.** and **Röhl, U.** (2017) Anatomy of Heinrich Layer 1 and its role in the last deglaciation. *Paleoceanography*, **32**, 284–303. https://doi.org/10.1002/2016PA003028

Holland, P.R., **Jenkins, A.** and **Holland, D.M.** (2010) Ice and ocean processes in the Bellingshausen Sea. *Antarctica. J. Geophys. Res*, **115**, C05020. https://doi.org/10.1029/2008JC005219s

Hubbard, S.M., **Covault, J.A.**, **Fildani, A.** and **Romans, B.W.** (2014) Sediment transfer and deposition in slope channels: Deciphering the record of enigmatic deep-sea processes from outcrop. *Geol. Soc. Am. Bull.*, **126**, 857–871. https://doi.org/10.1130/B30996.1

Hüneke, H., **Hernández-Molina, F.J.**, **Rodríguez-Tovar, F.J.**, **Llave, E.**, **Chiarella, D.**, **Mena, A.** and **Stow, D.A.V.** (2020) Diagnostic criteria using microfacies for calcareous contourites, turbidites and pelagites in the Eocene-Miocene slope succession, southern Cyprus. *Sedimentology*, **68**, 557–592. https://doi.org/10.1111/sed.12792

Hüneke, H. and **Stow, D.A.V.** (2008) Identification of ancient contourites: problems and palaeoceanographic significance. In: Contourites (Eds Rebesco, M. and Camerlenghi, A.), *Dev. Sedimentol.*, **60**, 323–344. doi: https://doi.org/10.1016/S0070-4571(08)10017-6

Ito, M. (2002) Kuroshio current-influenced sandy contourites from the Plio-Pleistocene Kazusa forearc basin, Boso Peninsula, Japan. *Geol. Soc. London Mem*, **22**, 421–432. https://doi.org/10.1144/GSL.MEM.2002.022.01.29

Ito, T., **Woloszyn, M.** and **Mazloff, M.** (2010) Anthropogenic carbon dioxide transport in the Southern Ocean driven by Ekman flow. *Nature*, **463**, 80–83. https://doi.org/10.1038/nature08687

Knaust, D. (2017) *Atlas of Trace Fossils in Well Core: Appearance, Taxonomy and Interpretation*. Springer, Switzerland, 209 pp. doi: https://doi.org/10.1007/978-3-319-49837-9

Laberg, J. and **Camerlenghi, A.** (2008) The significance of contourites for submarine slope stability. In: *Contourites* (Eds Rebesco, M. and Camerlenghi, A.), *Dev. Sedimentol.*, **60**, 537–556. doi:https://doi.org/10.1016/S0070-4571(08)10025-5

Larter, R.D. and **Barker, P.F.** (1989) Seismic stratigraphy of the Antarctic Peninsula Pacific margin: a record of Pliocene-Pleistocene ice volume and paleoclimate. *Geology*, **17**, 731–734. https://doi.org/10.1130/0091-7613(1989)017<0731:SSOTAP>2.3.CO;2

Larter, R.D. and **Barker, P.F.** (1991) Effects of ridge crest-trench interaction on Antarctic-Phoenix spreading: forces on a young subducting plate. *J. Geophys. Res.*, **96**, 583–607. https://doi.org/10.1029/91JB02053

Larter, R.D. and **Cunningham, A.P.** (1993) The depositional pattern and distribution of glacial-interglacial sequences on the Antarctic Peninsula Pacific margin. *Mar. Geol.*, **109**, 203–219. https://doi.org/10.1016/0025-3227(93)90061-Y

Larter, R.D., **Hogan**, K.A. and **Dowdeswell**, D.A. (2016) Large sediment drifts on the upper continental rise west of the Antarctic Peninsula. In: *Atlas of Submarine Glacial Landforms*: Modern, Quaternary and Ancient (Eds Dowdeswell, J.A., Canals, M., Jakobsson, M., Todd, B.J., Dowdeswell, E.K. and Hogan, K.A.), *Geol. Soc. London Mem.*, **46**, 401–402. https://doi.org/10.1144/M46.132

Larter, R.D., **Hogan, K.A.**, **Hillenbrand, C.-D.**, **Smith, J.A.**, **Batchelor, C.L.**, **Cartigny, M.**, **Tate, A.J.**, **Kirkham, J.D.**, **Roseby, Z.A.**, **Kuhn, G.**, **Graham, A.** and **Dowdeswell, J.A.** (2019) Subglacial hydrological control on flow of an Antarctic Peninsula palaeo-ice stream. *Cryosphere*, **13**, 1583–1596. https://doi.org/10.5194/tc-13-1583-2019

Larter, R.D., **Rebesco, M.**, **Vanneste, L.E.**, **Gambôa, L.A.P.** and **Barker, P.F.** (1997) Cenozoic tectonic, sedimentary and glacial history of the continental shelf west of Graham Land, Antarctic Peninsula. In: *Geology and Seismic Stratigraphy of the Antarctic Margin 2* (Eds Barker, P.F. and Cooper, A.K.), *Am. Geophys. Union Antarct. Res. Ser.*, **71**, 1–27. doi:https://doi.org/10.1029/AR071p0001

© 2022 The Authors. *Sedimentology* published by John Wiley & Sons Ltd on behalf of International Association of Sedimentologists, *Sedimentology*, **69**, 1953–1991

Lavoie, C., **Domack, E.W.**, **Pettit, E.C.**, **Scambos, T.A.**, **Larter, R.D.**, **Schenke, H.W.**, **Yoo, K.C.**, **Gutt, J.**, **Wellner, J.**, **Canals, M.**, **Anderson, M.** and **Amblas, D.** (2015) Configuration of the Northern Antarctic Peninsula Ice Sheet at LGM based on a new synthesis of seabed imagery. *Cryosphere*, **9**, 613–629. https://doi.org/10.5194/tc-9-613-2015

Livingstone, S.J., **Ó Cofaigh, C.**, **Stokes, C.R.**, **Hillenbrand, C.-D.**, **Vieli, A.** and **Jamieson, S.S.R.** (2012) Antarctic palaeo-ice streams. *Earth-Sci. Rev.*, **111**, 90–128. https://doi.org/10.1016/j.earscirev.2011.10.003

Lowe, D.R. (1982) Sediment gravity flows; II, depositional models with special reference to the deposits of high-density turbidity currents. *J. Sed. Petrol.*, **52**, 279–297. https://doi.org/10.1306/212F7F31-2B24-11D7-8648000102C1865D

Lozano, P., **Fernández-Salas, L.M.**, **Hernández-Molina, F.J.**, **Sánchez-Leal, R.**, **Sánchez-Guillamón, O.**, **Palomino, D.**, **Farias, C.**, **Mateo-Ramírez, Á.**, **López-González, N.**, **García, M.**, **Vázquez, J.-T.**, **Vila, Y.** and **Rueda, J.L.** (2020) Multiprocess interaction shaping geoforms and controlling substrate types and benthic community distribution in the Gulf of Cádiz. *Mar. Geol.*, **423**, 106139. https://doi.org/10.1016/j.margeo.2020.106139

Lucchi, R.G., **Camerlenghi, A.**, **Rebesco, M.**, **Colmenero-Hidalgo, E.**, **Sierro, F.J.**, **Sagnotti, L.**, **Urgeles, R.**, **Melis, R.**, **Morigi, C.**, **Bárcena, M.A.**, **Giorgetti, G.**, **Villa, G.**, **Persico, D.**, **Flores, J.A.**, **Rigual-Hernández, A.S.**, **Pedrosa, M.T.**, **Macrì, P.** and **Caburlotto, A.** (2013) Postglacial sedimentary processes on the Storfjorden and Kveithola trough mouth fans: significance of extreme glacimarine sedimentation. *Glob. Planet. Change*, **111**, 309–326. https://doi.org/10.1016/j.gloplacha.2013.10.008

Lucchi, R.G., **Rebesco, M.**, **Camerlenghi, A.**, **Busetti, M.**, **Tomadin, L.**, **Villa, G.**, **Persico, D.**, **Morigi, C.**, **Bonci, M.C.** and **Giorgetti, G.** (2002) Mid-late Pleistocene glacimarine sedimentary processes of a high-latitude, deep-sea sediment drift (Antarctic Peninsula Pacific margin). *Mar. Geol.*, **189**, 343–370. https://doi.org/10.1016/S0025-3227(02)00470-X

Lucchi, R.G. and **Rebesco, M.** (2007) Glacial contourites on the Antarctic Peninsula margin: insight for palaeoenvironmental and palaeoclimatic conditions. In: *Economic and Palaeoceanographic Significance of Contourite Deposits* (Eds Viana, A.R. and Rebesco, M.), *Geol. Soc. London Spec. Publ.*, **276**, 111–127. doi:https://doi.org/10.1144/GSL.SP.2007.276.01.06

Macrì, P., **Sagnotti, L.**, **Lucchi, R.G.** and **Rebesco, M.** (2006) A stacked record of relative geomagnetic paleointensity for the past 270 kyr from the western continental rise of the Antarctic Peninsula. *Earth Planet. Sci. Lett.*, **252**, 162–179. https://doi.org/10.1016/j.epsl.2006.09.037

Marchès, E., **Mulder, T.**, **Gonthier, E.**, **Cremer, M.**, **Hanquiez, V.**, **Garlan, T.** and **Lecroart, R.** (2010) Perched lobe formation in the gulf of Cadiz: interactions between gravity processes and contour currents (Algarve margin, southern Portugal). *Sed. Geol.*, **229**, 81–94. https://doi.org/10.1016/j.sedgeo.2009.03.008

Martín-Chivelet, J., **Fregenal-Martinez, M.A.** and **Chacon, B.** (2008) Traction structures in contourites. In: *Contourites* (Eds Rebesco, M. and Camerlenghi, A.), *Dev. Sedimentol.*, **60**, 157–182. doi: https://doi.org/10.1016/S0070-4571(08)10010-3

Martin-Puertas, C., **Tjallingii, R.**, **Bloemsma, M.** and **Brauer, A.** (2017) Varved sediment responses to early Holocene climate and environmental changes in Lake Meerfelder Maar (Germany) obtained from multivariate analyses of micro X-ray fluorescence core scanning data. *J. Quat. Sci.*, **32**, 427–436. https://doi.org/10.1002/jqs.2935

McCave, I.N. (2008) Size sorting during transport and deposition of fine sediments: sortable silt and flow speed. In: *Contourites* (Eds. Rebesco, M. and Camerlenghi, A.), *Dev. Sedimentol.*, **60**, 121–142. doi:https://doi.org/10.1016/S0070-4571(08)10008-5

McCave, I.N. and **Andrews, J.T.** (2019) Distinguishing current effects in sediments delivered to the ocean by ice. I. Principles, methods and examples. *Quatern. Sci. Rev.*, **212**, 92–107. https://doi.org/10.1016/j.quascirev.2019.03.031

McCave, I.N. and **Hall, I.R.** (2006) Size sorting in marine muds: processes, pitfalls, and prospects for paleo-flow speed proxies. *Geochem. Geophys. Geosys.*, **7**, Q10N05. https://doi.org/10.1029/2006GC001284

McCave, I.N., **Manighetti, B.** and **Robinson, S.G.** (1995) Sortable silt and fine sediment size/composition slicing: parameters for palaeocurrent speed and palaeoceanography. *Paleoceanography*, **10**, 593–610. https://doi.org/10.1029/94PA03039

McCave, I.N., **Thornalley, D.J.R.** and **Hall, I.R.** (2017) Relation of sortable silt grain-size to deep-sea current speeds: calibration of the 'Mud Current Meter'. *Deep-Sea Res.*, **127**, 1–12. https://doi.org/10.1016/j.dsr.2017.07.003

van der Meer, J.J.M. and **Menzies, J.** (2011) The micromorphology of unconsolidated sediments. *Sed. Geol.*, **238**, 213–232. https://doi.org/10.1016/j.sedgeo.2011.04.013

Mena, A., **Francés, G.**, **Pérez-Arlucea, M.**, **Hanebuth, T.J.**, **Bender, V.B.** and **Nombela, M.A.** (2018) Evolution of the Galicia Interior Basin over the last 60 ka: sedimentary processes and palaeoceanographic implications. *J. Quatern. Sci.*, **33**, 536–549. https://doi.org/10.1002/jqs.3032

Menzies, J. and **van der Meer, J.J.** (2018) Micromorphology and microsedimentology of glacial sediments chapter 21. In: *Past Glacial Environments* (Eds Menzies, J. and van der Meer, J.J.M.), 3rd edn, pp. 753–806. Elsevier, Amsterdam. https://doi.org/10.1016/B978-0-08-100524-8.00036-1

Michels, K.H., **Kuhn, G.**, **Hillenbrand, C.-D.**, **Diekmann, B.**, **Futterer, D.K.**, **Grobe, H.** and **Uenzelmann-Neben, G.** (2002) The southern Weddell Sea: Combined contourite-turbidite sedimentation at the southeastern margin of the Weddell Gyre. In: *Deep-Water Contourite Systems: Modern Drifts and Ancient Series, Seismic and Sedimentary Characteristics* (Eds Stow, D.A.V., Pudsey, C.J., Howe, J.A., Faugères, J.-C. and Viana, A.R.), *Geol. Soc. London Mem.*, **22**, 305–324. doi:https://doi.org/10.1144/GSL.MEM.2002.022.01.22

Michels, K.H., **Rogenhagen, J.** and **Kuhn, G.** (2001) Recognition of contour-current influence in mixed contourite-turbidite sequences of the western Weddell Sea, Antarctica. *Mar. Geophys. Res.*, **22**, 465–485. https://doi.org/10.1023/A:1016303817273

Middleton, G.V. and **Hampton, M.A.** (1973) Sediment gravity flows: mechanics of flow and deposition. In: *Turbidity and Deep-Water Sedimentation* (Eds Middleton, G.V. and Bouma, A.H.), *SEPM, Pacific Section, Short Course Lecture Notes*, Anaheim, 1–38.

Miguez-Salas, O., **Dorador, J.** and **Rodríguez-Tovar, F.J.** (2019) Introducing Fiji and ICY image processing

© 2022 The Authors. *Sedimentology* published by John Wiley & Sons Ltd on behalf of International Association of Sedimentologists, *Sedimentology*, **69**, 1953–1991

techniques in ichnological research as a tool for sedimentary basin analysis. *Mar. Geol.*, **413**, 1–9. https://doi.org/10.1016/j.margeo.2019.03.013

Miramontes, E., **Garziglia, S.**, **Sultan, N.**, **Jouet, G.** and **Cattaneo, A.** (2018) Morphological control of slope instability in contourites: a geotechnical approach. *Landslides*, **15**, 1085–1095. https://doi.org/10.1007/s10346-018-0956-6

Miramontes, E., **Penven, P.**, **Fierens, R.**, **Droz, L.**, **Toucanne, S.**, **Jorry, S.J.**, **Jouet, G.**, **Pastor, L.**, **Jacinto, R.S.**, **Gaillot, A.**, **Giraudeau, J.** and **Raisson, F.** (2019) The influence of bottom currents on the Zambezi Valley morphology (Mozambique Channel, SW Indian Ocean): In situ current observations and hydrodynamic modelling. *Mar. Geol.*, **410**, 42–55. https://doi.org/10.1016/j.margeo.2019.01.002

Moerz, T. and **Wolf-Welling, T.C.W.** (2001) Data report: Fine-fraction grain-size distribution data and their statistical treatment and relation to processes, Site 1095 (ODP Leg 178, western Antarctic Peninsula). In: *Proc. ODP Sci. Results* (Eds Barker, P.F., Camerlenghi, A., Acton, G.D. and Ramsay, A.T.S.), **178**, 1–25.

Mulder, T., **Faugères, J.-C.** and **Gonthier, E.** (2008) Mixed Turbidite-Contourite systems. In: *Contourites* (Eds Rebesco, M. and Camerlenghi, A.), *Dev. Sedimentol.*, **60**, 435–456. doi:https://doi.org/10.1016/S0070-4571(08)10021-8

Mulder, T. and **Hüneke, H.** (2014) Turbidite. In: *Encyclopedia of Marine Geosciences* (Eds Harff, J., Meschede, M., Petersen, S. and Thiede, J.). Springer, Dordrecht. doi:https://doi.org/10.1007/978-94-007-6644-0_145-1

Mutti, E. (1992) *Turbidite sandstones*. Istituto di geologia, Università di Parma & AGIP, 275 pp.

Mutti, E. (2011) Turbidites. Search and Discovery Article #30214.

Mutti, E., **Cunha, R.S.**, **Bulhoes, E.M.**, **Arienti, L.M.** and **Viana, A.R.** (2014) Contourites and Turbidites of the Brazilian Marginal Basins. Search and Discovery Article #51069.

Naveira Garabato, A.C., **Heywood, K.J.** and **Stevens, D.P.** (2002) Modification and pathways of Southern Ocean Deep Waters in the Scotia Sea. *Deep-Sea Res.*, **49**, 681–705. https://doi.org/10.1016/S0967-0637(01)00071-1

Naveira Garabato, A.C., **Stevens, D.P.** and **Heywood, K.J.** (2003) Water mass convection, fluxes and mixing in the Scotia Sea diagnosed by an inverse model. *J. Phys. Oceanogr.*, **33**, 2565–2587. https://doi.org/10.1175/1520-0485(2003)033<2565:WMCFAM>2.0.CO;2

Nerlich, R., **Clark, S.R.** and **Bunge, H.-P.** (2013) The Scotia Sea gateway: no outlet for Pacific mantle. *Tectonophysics*, **604**, 41–50. https://doi.org/10.1016/j.tecto.2012.08.023

Ó Cofaigh, C., **Davies, B.J.**, **Livingstone, S.J.**, **Smith, J.A.**, **Johnson, J.S.**, **Hocking, E.P.**, **Hodgson, D.A.**, **Anderson, J.B.**, **Bentley, M.J.**, **Canals, M.**, **Domack, E.**, **Dowdeswell, J.A.**, **Evans, J.**, **Glasser, N.F.**, **Hillenbrand, C.-D.**, **Larter, R.D.**, **Roberts, S.J.** and **Simms, A.R.** (2014) Reconstruction of ice-sheet changes in the Antarctic Peninsula since the Last Glacial Maximum. *Quatern. Sci. Rev.*, **100**, 87–100. https://doi.org/10.1016/j.quascirev.2014.06.023

Ó Cofaigh, C., **Dowdeswell, J.A.** and **Pudsey, C.J.** (2001) Late Quaternary iceberg rafting along the Antarctic Peninsula continental rise and in the Weddell and Scotia Seas. *Quatern. Res.*, **56**, 308–321. https://doi.org/10.1006/qres.2001.2267

Orsi, A.H., **Johnson, G.C.** and **Bullister, J.L.** (1999) Circulation, mixing, and production of Antarctic bottom water. *Prog. Oceanogr.*, **43**, 55–109. https://doi.org/10.1016/S0079-6611(99)00004-X

Orsi, A.H., **Whitworth III, T.** and **Nowlin Jr., W.D.** (1995) On the meridional extent and fronts of the Antarctic circumpolar current. *Deep-Sea Res.*, **42**, 641–673. https://doi.org/10.1016/0967-0637(95)00021-W

Palamenghi, L., **Keil, H.** and **Spiess, V.** (2015) Sequence stratigraphic framework of a mixed turbidite-contourite depositional system along the NW slope of the South China Sea. *Geo-Mar. Lett.*, **35**, 1–21. https://doi.org/10.1007/s00367-014-0385-z

Palmer, A.P., **Lee, J.A.**, **Kemp, R.A.** and **Carr, S.J.** (2008) *Revised laboratory procedures for the preparation of thin sections from unconsolidated material*. Unpubl. Intern. Rep. Royal Holloway, University of London.

Palmer, M., **Gomis, D.**, **Flexas, M.D.M.**, **Jordà, G.**, **Jullion, L.**, **Tsubouchi, T.** and **Naveira-Garabato, A.C.** (2012) Water mass pathways and transports over the South Scotia Ridge west of 50°W. *Deep-Sea Res.*, **59**, 8–24. https://doi.org/10.1016/j.dsr.2011.10.005

Pandolpho, B.T., **Klein, A.H.F.**, **Dutra, I.**, **Mahiques, M.M.**, **Viana, A.R.**, **Bueno, G.V.**, **Machado, A.A.**, **Camargo, Y.L.**, **Hercos, C.M.**, **Lima, Y.**, **Filho, A.F.** and **Theodoro, C.E.** (2021) Seismic record of a cyclic turbidite-contourite system in the Northern Campos Basin, SE Brazil. *Mar. Geol.*, **434**, 106422. https://doi.org/10.1016/j.margeo.2021.106422

Pankhurst, R.J. (1990) The Paleozoic and Andean magmatic arcs of West Antarctica and southern South America. *Geol. Soc. Am. Spec. Publ.*, **241**, 1–7. https://doi.org/10.1130/SPF41-p1

Patterson, S.L. and **Whitworth, T.** (1990) Physical oceanography. In: *Antarctic Sector of the Pacific, Elsevier Oceanogr. Series* (Ed. Glasby, G.P.), pp. 55–93. Elsevier, Amsterdam. https://doi.org/10.1016/S0422-9894(08)70517-8

Poblete, E., **Arriagada, C.**, **Roperch, P.**, **Astudillo, N.**, **Hervé, F.**, **Kraus, S.** and **Le Roux, J.P.** (2011) Paleomagnetism and tectonics of the South Shetland Islands and the northern Antarctic Peninsula. *Earth Planet. Sci. Lett.*, **302**, 299–313. https://doi.org/10.1016/j.epsl.2010.12.019

Postma, G. (1986) Classification of sediment gravity flow deposits based on flow conditions during sedimentation. *Geology*, **14**, 291–294. https://doi.org/10.1130/0091-7613(1986)14<291:CFSGDB>2.0.CO;2

Postma, G., **Cartigny, M.B.** and **Kleverlaan, K.** (2009) Structureless, coarse-tail graded Bouma Ta formed by internal hydraulic jump of the turbidity current? *Sed. Geol.*, **219**, 1–6. https://doi.org/10.1016/j.sedgeo.2009.05.018

Postma, G. and **Kleverlaan, K.** (2018) Supercritical flows and their control on the architecture and facies of small-radius sand-rich fan lobes. *Sed. Geol.*, **364**, 53–70. https://doi.org/10.1016/j.sedgeo.2017.11.015

Pudsey, C.J. (2000) Sedimentation on the continental rise west of the Antarctic Peninsula over the last three glacial cycles. *Mar. Geol.*, **167**, 313–338. https://doi.org/10.1016/S0025-3227(00)00039-6

Pudsey, C.J. (2002) Neogene record of Antarctic Peninsula glaciation in continental rise sediments: ODP Leg 178, Site 1095. In: *Proc. ODP Sci. Results* (Eds. Barker, P.F., Camerlenghi, A., Acton, G.D. and Ramsay, A.T.S.), **178**, 1–25. doi:https://doi.org/10.2973/odp.proc.sr.178.214.2001

Pudsey, C.J. and **Camerlenghi, A.** (1998) Glacial-interglacial deposition on a sediment drift on the Pacific margin of the

Antarctic Peninsula. *Antarct. Sci.*, **10**, 286–308. https://doi.org/10.1017/S0954102098000376

Rasmussen, S.L., **Lykke-Andersen, H.**, **Kuijpers, A.** and **Troelstra, S.R.** (2003) Post-Miocene sedimentation at the continental rise of Southeast Greenland: the interplay between turbidity and contour currents. *Mar. Geol.*, **196**, 37–52. https://doi.org/10.1016/S0025-3227(03)00043-4

Rebesco, M., **Camerlenghi, A.** and **Zanolla, C.** (1998) Bathymetry and morphogenesis of the continental margin west of the Antarctic Peninsula. *Terra Antartica*, **5**, 715–725.

Rebesco, M. and **Camerlenghi, A.** (2008) Late Pliocene margin development and mega debris flow deposits on the Antarctic continental margins: evidence of the onset of the modern Antarctic Ice Sheet? *Palaeogeo. Palaeoclimatol. Palaeoecol.*, **260**, 149–167. https://doi.org/10.1016/j.palaeo.2007.08.009

Rebesco, M., **Hernández-Molina, F.J.**, **Van Rooij, D.** and **Wåhlin, A.** (2014) Contourites and associated sediments controlled by deep-water circulation processes: state-of-the-art and future considerations. *Mar. Geol.*, **352**, 111–154. https://doi.org/10.1016/j.margeo.2014.03.011

Rebesco, M., **Larter, R.D.**, **Camerlenghi, A.** and **Barker, P.F.** (1996) Giant sediment drifts on the continental rise west of the Antarctic Peninsula. *Geo-Mar. Lett.*, **16**, 65–75. https://doi.org/10.1007/BF02202600

Rebesco, M., **Pudsey, C.**, **Canals, M.**, **Camerlenghi, A.**, **Barker, P.**, **Estrada, F.** and **Giorgetti, A.** (2002) Sediment drift and deep-sea channel systems, Antarctic Peninsula Pacific Margin. In: *Deep-water Contourite Systems: Modern Drifts and Ancient Series, Seismic and Sedimentary Characteristics* (Eds Stow, D.A.V., Pudsey, C.J., Howe, J.A., Faugères, J.-C. and Viana, A.R.), *Geol. Soc. London Mem.*, **22**, 353–371. doi:https://doi.org/10.1144/GSL.MEM.2002.022.01.25

Rodrigues, S., **Hernández-Molina, F.J.** and **Kirby, A.** (2021) Late Cretaceous hybrid (turbidite-contourite) system along the Argentine Margin: paleoceanographic and conceptual implications. *Mar. Petrol. Geol.*, **123**, 104768. https://doi.org/10.1016/j.marpetgeo.2020.104768

Rodríguez-Tovar, F.J., **Dorador, J.**, **Grunert, P.** and **Hodell, D.** (2015a) Deep-sea trace fossil and benthic foraminiferal assemblages across glacial terminations 1, 2 and 4 at the 'Shackleton Site' (IODP Expedition 339, Site U1385). *Glob. Planet. Change*, **133**, 359–370. https://doi.org/10.1016/j.gloplacha.2015.05.003

Rodríguez-Tovar, F.J., **Dorador, J.**, **Martín-García, G.M.**, **Sierro, F.J.**, **Flores, J.A.** and **Hodell, D.A.** (2015b) Response of macrobenthic and foraminifer communities to changes in deep-sea environmental conditions from Marine Isotope Stage (MIS) 12 to 11 at the 'Shackleton Site'. *Glob. Planet. Change*, **133**, 176–187. https://doi.org/10.1016/j.gloplacha.2015.08.012

Rodríguez-Tovar, F.J., **Dorador, J.** and **Hodell, D.A.V.** (2019) Trace fossils evidence of a complex history of nutrient availability and oxygen conditions during Heinrich Event 1. *Glob. Planet. Change*, **174**, 26–34. https://doi.org/10.1016/j.gloplacha.2019.01.003

Rodríguez-Tovar, F.J., **Dorador, J.**, **Mena, A.** and **Francés, G.** (2020) Regional and global changes during Heinrich Event 1 affecting macrobenthic habitat: ichnological evidence of sea-bottom conditions at the Galicia Interior Basin. *Glob. Planet. Change*, **192**, 103227. https://doi.org/10.1016/j.gloplacha.2020.103227

Rodríguez-Tovar, F.J. and **Hernández-Molina, F.J.** (2018) Ichnological analysis of contourites: past, present and future. *Earth-Sci. Rev.*, **182**, 28–41. https://doi.org/10.1016/j.earscirev.2018.05.008

Rodríguez-Tovar, F.J., **Nagy, J.** and **Reolid, M.** (2014) Palaeoenvironment of Eocene prodelta in Spitsbergen recorded by the trace fossil *Phycosiphon incertum*. *Polar Res.*, **33**, 23786. https://doi.org/10.3402/polar.v33.23786

Sagnotti, L.P., **Macrì, P.**, **Camerlenghi, A.** and **Rebesco, M.** (2001) Environmental magnetism of late Pleistocene sediments from the Pacific margin of the Antarctic Peninsula and interhemispheric correlation of climatic events. *Earth Planet. Sci. Lett.*, **192**, 65–80. https://doi.org/10.1016/S0012-821X(01)00438-1

Salabarnada, A., **Escutia, C.**, **Röhl, U.**, **Hans Nelson, C.**, **McKay, R.**, **Jiménez-Espejo, F.J.**, **Bijl, P.K.**, **Hartman, J.D.**, **Strother, S.L.**, **Salzmann, U.**, **Evangelinos, D.**, **López-Quirós, A.**, **Flores, J.A.**, **Sangiorgi, F.**, **Ikehara, M.** and **Brinkhuis, H.** (2018) Paleoceanography and ice sheet variability offshore Wilkes Land, Antarctica – part 1: insights from late Oligocene astronomically paced contourite sedimentation. *Clim. Past*, **14**, 991–1014. https://doi.org/10.5194/cp-14-991-2018

Sansom, P. (2018) Hybrid turbidite-contourite systems of the Tanzanian margin. *Geol. Soc. Lond. Petrol. Geosci.*, **24**, 258–276. https://doi.org/10.1144/petgeo2018-044

Shanmugam, G. (1997) The Bouma sequence and the turbidite mind set. *Earth-Sci. Rev.*, **42**, 201–229. https://doi.org/10.1016/S0012-8252(97)81858-2

Shanmugam, G. (2016) Slides, slumps, debris flows, turbidity currents, and bottom currents. In: *Reference Module in Earth Systems and Environmental Sciences* (Eds Kirk Cochran, J., Bokuniewicz, H.J. and Yager, P.L.). Elsevier, Amsterdam, 4 pp. https://doi.org/10.1016/B978-0-12-409548-9.04380-3

Shanmugam, G. (2017) Contourites: physical oceanography, process sedimentology, and petroleum geology. *Petrol. Explor. Dev.*, **44**, 183–216. https://doi.org/10.1016/S1876-3804(17)30023-X

Shanmugam, G., **Spalding, T.D.** and **Rofheart, D.H.** (1993) Process sedimentology and reservoir quality of deep-marine bottom current reworked sands (sandy contourites), an example from the Gulf of Mexico. *AAPG Bull.*, **77**, 1241–1259. https://doi.org/10.1306/BDFF8E52-1718-11D2-8645000102C1865D

Sievers, H.A. and **Nowlin Jr., W.D.** (1984) The stratification and water masses at Drake Passage. *J. Geophys. Res.*, **89**, 10489–10514. https://doi.org/10.1029/JC089iC06p10489

Spofforth, D.J.A., **Pälike, H.** and **Green, D.** (2008) Paleogene record of elemental concentrations in sediments from the Arctic Ocean obtained by XRF analyses. *Paleoceanography*, **23**, PA1S09. https://doi.org/10.1029/2007PA001489

Stanley, D.J. (1987) Turbidite to current-reworked sand continuum in Upper cretaceous rocks, U.S. Virgin Islands. *Mar. Geol.*, **78**, 143–151. https://doi.org/10.1016/0025-3227(87)90073-9

Stanley, D.J. (1988) Turbidites reworked by bottom currents: upper cretaceous examples from St. Croix, US Virgin Islands. Smithsonian contributions to the marine sciences. *Mar. Sci.*, **33**, 85. https://doi.org/10.5479/si.01960768.33

Stanley, D.J. (1993) Model for turbidite-to-contourite continuum and multiple process transport in deep marine settings: examples in the rock record. *Sed. Geol.* **82**, 241–255. https://doi.org/10.1016/0037-0738(93)90124-N

Stow, D.A.V. (1982) Bottom currents and contourites in the North Atlantic. *Bull. Inst. Géol. Bassin Aquitaine*, **31**, 151–166.

© 2022 The Authors. *Sedimentology* published by John Wiley & Sons Ltd on behalf of International Association of Sedimentologists, *Sedimentology*, **69**, 1953–1991

Stow, D.A.V., **Faugères, J.-C.**, **Viana, A.R.** and **Gonthier, E.** (1998) Fossil contourites: a critical review. *Sed. Geol.*, **115**, 3–31. https://doi.org/10.1016/S0037-0738(97)00085-7

Stow, D.A.V. and **Faugères, J.-C.** (2008) Contourites facies and the facies model. In: *Contourites* (Eds. Rebesco, M. and Camerlenghi, A.), *Dev. Sedimentol.*, **60**, 223–256. https://doi.org/10.1016/S0070-4571(08)10013-9

Stow, D.A.V., **Hernández-Molina, F.J.**, **Llave, E.**, **Sayago-Gil, M.**, **Díaz del Rio, V.** and **Branson, A.** (2009) Bedform-velocity matrix: the estimation of bottom current velocity from bedform observations. *Geology*, **37**, 327–330. https://doi.org/10.1130/G25259A.1

Stow, D.A.V. and **Piper, D.J.W.** (1984) Deep-water fine-grained sediments: facies models. *Geol. Soc. London Spec. Publ.*, **15**, 611–646. https://doi.org/10.1144/GSL.SP.1984.015.01.38

Stow, D.A.V., **Pudsey, C.J.**, **Howe, J.A.**, **Faugères, J.-C.** and **Viana, A.R.** (2002) Deep-water contourite systems: modern drifts and ancient series, seismic and sedimentary characteristics. *Geol. Soc. London Mem.*, **22**, 457. https://doi.org/10.1144/GSL.MEM.2002.022

Stow, D.A.V. and **Smillie, Z.** (2020) Distinguishing between deep-water sediment facies: turbidites, contourites and hemipelagites. *Geosciences*, **10**, 68. https://doi.org/10.3390/geosciences10020068

Stow, D.A.V. and **Tabrez, A.R.** (1998) Hemipelagites: processes, facies and model. *Geol. Soc. London Spec. Publ.*, **129**, 317–337. https://doi.org/10.1144/GSL.SP.1998.129.01.19

Stramma, L. and **England, M.** (1999) On the water masses and mean circulation of the South Atlantic Ocean. *J. Geophys. Res.*, **104**, 20863–20883. https://doi.org/10.1029/1999JC900139

Tallobre, C., **Giresse, P.**, **Bassetti, M.-A.**, **Loncke, L.**, **Bayon, G.**, **Buscail, R.**, **Tudryn, A.** and **Zaragosi, S.** (2019) Formation and evolution of glauconite in the Demerara Contourite depositional system related to NADW circulation changes during late Quaternary (French Guiana). *J. S. Am. Earth Sci.*, **92**, 167–183. https://doi.org/10.1016/j.jsames.2019.03.011

Teixeira, M., **Terrinha, P.**, **Roque, C.**, **Rosa, M.**, **Ercilla, G.** and **Casas, D.** (2019) Interaction of alongslope and downslope processes in the Alentejo Margin (SW Iberia) – implications on slope stability. *Mar. Geol.*, **410**, 88–108. https://doi.org/10.1016/j.margeo.2018.12.011

Thiéblemont, A., **Hernández-Molina, F.J.**, **Ponte, J.-P.**, **Robin, C.**, **Guillocheau, F.**, **Cazzola, C.** and **Raisson, F.** (2020) Seismic stratigraphic framework and depositional history for Cretaceous and Cenozoic contourite depositional systems of the Mozambique Channel. *SW Indian Ocean. Mar. Geol.*, **425**, 106192. https://doi.org/10.1016/j.margeo.2020.106192

Tomlinson, J.S., **Pudsey, C.J.**, **Livermore, R.A.**, **Larter, R.D.** and **Barker, P.F.** (1992) Long-range Sidescan Sonar (GLORIA) Survey of the Antarctic Peninsula Pacific Margin. In: *Recent Progress in Antarctic Earth Science* (Eds Yoshida, Y., Kaminuma, K. and Shiraishi, K.), pp. 423–430. Terra Scientific Publishing Company, Tokyo.

Tucholke, B.E. (1977) Sedimentation process and acoustic stratigraphy in the Bellingshausen Basin. *Mar. Geol.*, **25**, 209–230. https://doi.org/10.1016/0025-3227(77)90053-6

Tucholke, B.E. and **Houtz, R.E.** (1976) Sedimentary framework of the Bellingshausen basin from seismic profiler data. *Init. Rep. DSDP*, **35**, 197–228. https://doi.org/10.2973/dsdp.proc.35.107.1976

Uenzelmann-Neben, G. (2006) Depositional patterns at Drift 7, Antarctic Peninsula: along-slope versus down-slope sediment transport as indicators for oceanic currents and climatic conditions. *Mar. Geol.*, **233**, 49–62. https://doi.org/10.1016/j.margeo.2006.08.008

Vandorpe, T., **Collart, T.**, **Cnudde, V.**, **Lebreiro, S.**, **Hernández-Molina, F.J.**, **Alonso, B.**, **Mena, A.**, **Antón, L.** and **Van Rooij, D.** (2019) Quantitative characterisation of contourite deposits using medical CT. *Mar. Geol.*, **417**, 106003. https://doi.org/10.1016/j.margeo.2019.106003

Vanneste, L.E. and **Larter, R.D.** (1995) Deep-tow boomer survey on the Antarctic Peninsula Pacific margin: An investigation of the morphology and acoustic characteristics of Late Quaternary sedimentary deposits on the outer continental shelf and upper slope. In: *Geology and Seismic Stratigraphy of the Antarctic Margin* (Eds Cooper, A.K., Barker, P.F. and Brancolini, G.), *Antarct. Res. Ser.*, **68**, 97–121. https://doi.org/10.1029/AR068p0097

Vautravers, M.J., **Hodell, D.A.**, **Channell, J.**, **Hillenbrand, C.-D.**, **Hall, M.**, **Smith, J.** and **Larter, R.D.** (2013) Palaeoenvironmental records from the West Antarctic Peninsula drift sediments over the last 75. In: *Antarctic Palaeoenvironments and Earth-Surface Processes* (Eds Hambrey, M.J., Barker, P.F., Barrett, P.J., Bowman, V., Davies, B., Smellie, J.L. and Tranter, M.), *Geol. Soc. London Spec. Publ.*, **381**, 263–276. https://doi.org/10.1144/SP381.12

Venuti, A., **Florindo, F.**, **Caburlotto, A.**, **Hounslow, M.W.**, **Hillenbrand, C.-D.**, **Strada, E.**, **Talarico, F.M.** and **Cavallo, A.** (2011) Late Quaternary sediments from deep-sea sediment drifts on the Antarctic Peninsula Pacific margin: climatic control on provenance of minerals. *J. Geophys. Res.*, **116**, B06104. https://doi.org/10.1029/2010JB007952

Viana, A.R. (2008) Economic relevance of contourites. In: *Contourites* (Eds Rebesco, M. and Camerlenghi, A.), *Dev. Sedimentol.*, **60**, 493–510. https://doi.org/10.1016/S0070-4571(08)10023-1

Viana, A.R., **Faugères, J.-C.** and **Stow, D.A.V.** (1998) Bottom current controlled sand deposits – a review of modern shallow- to deep-water environments. *Sed. Geol.*, **115**, 53–80. https://doi.org/10.1016/S0037-0738(97)00087-0

Villa, G., **Persico, D.**, **Bonci, M.C.**, **Lucchi, R.G.**, **Morigi, C.** and **Rebesco, M.** (2003) Biostratigraphic characterization and Quaternary microfossil palaeoecology in sediment drifts west of the Antarctic Peninsula – implications for cyclic glacial-interglacial deposition. *Palaeogeogr. Palaeoclimatol. Palaeoecol.*, **198**, 273–263. https://doi.org/10.1016/S0031-0182(03)00403-6

Volpi, V., **Amblas, D.**, **Camerlenghi, A.**, **Canals, M.**, **Rebesco, M.** and **Urgeles, R.** (2011) Late Neogene to Recent Seafloor Instability on the Deep Pacific Margin of the Antarctic Peninsula. In: *Mass-Transport Deposits in Deepwater Settings* (Eds Shipp, R.C., Weimer, P. and Posamentier, H.W.), *SEPM Spec. Publ.*, **96**. https://doi.org/10.2110/sepmsp.096.161

de Weger, W., **Hernández-Molina, F.J.**, **Miguez-Salas, O.**, **de Castro, S.**, **Bruno, M.**, **Chiarella, D.**, **Sierro, F.J.**, **Blackbourn, G.** and **Manar, M.A.** (2021) Contourite depositional system after the exit of a strait: case study from the late Miocene South Rifian Corridor, Morocco. *Sedimentology*, **68**, 2996–3032. https://doi.org/10.1111/sed.12882

Weltje, G.J. and **Tjallingii, R.** (2008) Calibration of XRF core scanners for quantitative geochemical logging of sediment

© 2022 The Authors. *Sedimentology* published by John Wiley & Sons Ltd on behalf of International Association of Sedimentologists, *Sedimentology*, **69**, 1953–1991

cores: theory and application. *Earth Planet. Sci. Lett.*, **274**, 423–438. https://doi.org/10.1016/j.epsl.2008.07.054

Whitworth III, T. and **Nowlin Jr., W.D.** (1987) Water masses and currents of the Southern Ocean at the Greenwich Meridian. *J. Geophys. Res.*, **92**, 6462–6476. https://doi.org/10.1029/JC092iC06p06462

Whitworth III, T., **Orsi, A.H.**, **Kim, S.-J.** and **Nowlin Jr., W.D.** (1998) Water masses and mixing near the Antarctic Slope Front. *Antarct. Res. Ser.*, **75**, 1–27. https://doi.org/10.1029/AR075p0001

Wright, R. and **Anderson, J.B.** (1982) The importance of sediment gravity flow to sediment transport and sorting in a glacial marine environment: Eastern Weddell Sea, Antarctica. *GSA Bull.*, **93**, 951–963. https://doi.org/10.1130/0016-7606(1982)93<951:TIOSGF>2.0.CO;2

Wu, L., **Wilson, D.J.**, **Wang, R.**, **Yin, X.**, **Chen, Z.**, **Xiao, W.** and **Huang, M.** (2020) Evaluating Zr/Rb ratio from XRF scanning as an indicator of grain-size variations of glaciomarine sediments in the southern ocean. *Geochem. Geophys. Geosyst.*, **21**, e2020GC009350. https://doi.org/10.1029/2020GC009350

Zhang, L.-F., **Pan, M.** and **Li, Z.-L.** (2020) 3D modeling of deepwater turbidite lobes: a review of the research status and progress. *Petrol. Sci.*, **17**, 317–333. https://doi.org/10.1007/s12182-019-00415-y

Manuscript received 22 July 2021; revision accepted 27 January 2022

Supporting Information

Additional information may be found in the online version of this article:

Fig S1. (A) Map of the Pacific margin of the Antarctic Peninsula (PMAP) with schematic deep-water circulation after Orsi *et al.* (1995, 1999), Giorgetti *et al.* (2003), Hillenbrand *et al.* (2008a), Holland *et al.* (2010), Palmer *et al.* (2012) and Hernández-Molina *et al.* (2017). (B) Temperature–salinity plot for the water masses on the PMAP.

Fig S2a. Detailed lithological logs and facies interpretations of the sediment cores examined in this study.

Fig S2b. (continuation).

Fig S3. Chronological constraints provided by previously published relative palaeointensity (RPI) studies for the JR298 cores (Channell *et al.*, 2019) and the SEDANO cores (Venuti *et al.*, 2011).

Table S1. Marine Isotope Stage (MIS) boundaries for all the studied cores. MIS of the SEDANO cores after Lucchi *et al.* (2002) and Lucchi and Rebesco (2007) and of the JR298 cores after Channell *et al.* (2019) and Hillenbrand *et al.* (2021). PC: piston core; GBC: giant box core.

Supinfo S1. Marine Isotope Stage (MIS) boundaries for all the studied cores.

© 2022 The Authors. *Sedimentology* published by John Wiley & Sons Ltd on behalf of International Association of Sedimentologists, *Sedimentology*, **69**, 1953–1991